# Touchdown and Pull-In Voltage Behavior of a MEMS Device with Varying Dielectric Properties

Y. GUO, Z. PAN, and M. J. WARD

*Dept. of Mathematics, University of British Columbia, Vancouver, Canada V6T 1Z2 (corresponding author: M. J. Ward)*

(*Received 11 March 2005*)

The pull-in voltage instability associated with a simple MEMS device, consisting of a thin dielectric elastic membrane supported above a rigid conducting ground plate, is analyzed. The upper surface of the membrane is coated with a thin conducting film. In a certain asymptotic limit representing a thin device, the mathematical model consists of a nonlinear partial differential equation for the deflection of the thin dielectric membrane. When a voltage $V$ is applied to the conducting film, the dielectric membrane deflects towards the bottom plate. For a slab, a circular cylindrical, and a square domain, numerical results are given for the saddle-node bifurcation value $V_*$, also referred to as the pull-in voltage, for which there is no steady-state membrane deflection for $V > V_*$. For $V > V_*$ it is shown numerically that the membrane dynamics are such that the thin dielectric membrane touches the lower plate in finite time. Results are given for both spatially uniform and nonuniform dielectric permittivity profiles in the thin dielectric membrane. By allowing for a spatially nonuniform permittivity profile, it is shown that the pull-in voltage instability can be delayed until larger values of $V$ and that greater pull-in distances can be achieved. Analytical bounds are given for the pull-in voltage $V_*$ for two classes of spatially variable permittivity profiles. In particular, a rigorous analytical bound $V_1$, which depends on the class of permittivity profile, is derived that guarantees for the range $V > V_1 > V_*$ that there is no steady-state solution for the membrane deflection and that finite-time touchdown occurs. Numerical results for touchdown behavior, both for $V > V_1$ and for $V_* < V < V_1$, together with an asymptotic construction of the touchdown profile, are given for both a spatially uniform and a spatially nonuniform permittivity profile.

Key words: quenching, pull-in voltage, saddle-node, MEMS, dielectric permittivity.

## 1 Introduction

Micro-Electromechanical Systems (MEMS) combine electronics with micro-size mechanical devices to design various types of microscopic machinery. MEMS devices are key components of many commercial systems including, accelerometers for airbag deployment in automobiles, ink jet printer heads, and chemical sensors. Mathematical models of physical phenomena associated with the rapidly developing field of MEMS technology are discussed in [**13**].

A key component of many MEMS systems is the simple device shown in Fig. 1. The upper part of this device consists of a thin deformable elastic membrane that is held fixed along its boundary. This membrane is modeled as a dielectric of a thin, but finite, thickness. The upper surface of this membrane is coated with a negligibly thin metallic conducting film. The thin dielectric membrane lies above a rigid inelastic conducting ground plate. When a voltage $V$ is applied to the conducting film, the thin dielectric membrane deflects towards the ground plate. A similar deflection phenomenon, but on a macroscopic length scale, occurs in the field of electrohydrodynamics. In this context, G.I. Taylor [**17**] studied the electrostatic deflection of two oppositely charged soap films, and he predicted a critical voltage for which the two soap films would touch together.

A similar physical limitation on the applied voltage occurs for the MEMS device of Fig. 1 in that there is a

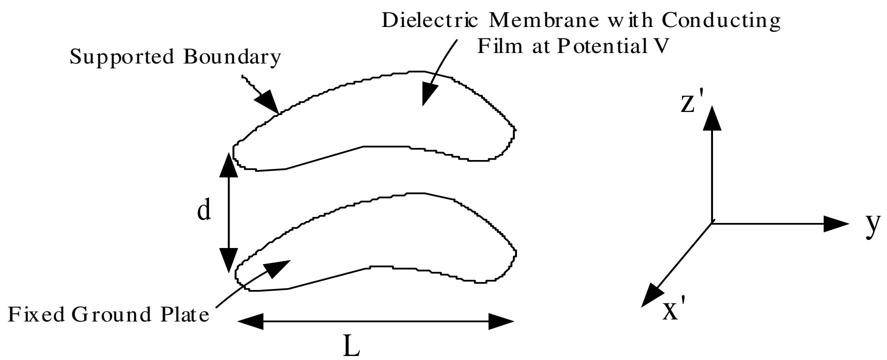


FIGURE 1. The MEMS capacitor. The upper surface of the elastic membrane is coated with an ultra-thin conducting film.

maximum voltage, called the pull-in voltage $V_*$, that can be safely applied to the system. More specifically, if the applied voltage $V$ is increased past $V_*$ there is no longer a steady-state solution for the membrane deflection (cf. [**11**], [**14**]). The existence of such a pull-in voltage was first demonstrated for a lumped mass-spring model of electrostatic actuation in the pioneering study of [**10**], where the restoring force of the deflected membrane is modeled by a Hookean spring. In this lumped model the attractive inverse square law electrostatic force between the membrane and the ground plate dominates the restoring force of the spring for small gap sizes and large applied voltages. This leads to a touchdown or snap-through behavior whereby the membrane hits the ground plate when the applied voltage is sufficiently large. Although the lumped model qualitatively predicts the existence of a pull-in voltage and the snap-through phenomenon it cannot quantitatively account for details such as membrane geometry etc.

A more detailed mathematical model of this phenomena, leading to a partial differential equation (PDE) for the dimensionless deflection $u$ of the membrane, was derived and analyzed in [**6**], [**11**], [**12**], [**14**], and [**15**] (see also the references therein). In the damping-dominated limit, and by modeling the thin dielectric as a membrane with zero rigidity, a narrow-gap asymptotic analysis was used in [**6**] and [**14**] to derive that $u$ satisfies

$$\frac{\partial u}{\partial t} = \Delta u - \frac{\lambda f(x,y)}{(1+u)^2}\,, \quad x \in \Omega\,; \qquad u = 0\,, \quad (x,y) \in \partial\Omega\,; \qquad u(x,y,0) = 0\,. \tag{1.1}$$

An outline of the derivation of (1.1) following that detailed in [**14**] and [**6**] is given in Appendix A. In (1.1), $\lambda$ characterizes the relative strength of electrostatic and mechanical forces in the system, and is given by

$$\lambda = \frac{\varepsilon_0 V^2 L^2}{2Td^3}\,. \tag{1.2}$$

Here $V$ is the applied voltage, $d$ is the undeflected gap size (see Fig. 1), $L$ and $T$ are the length scale and tension of the membrane, respectively, and $\varepsilon_0$ is the permittivity of free space. In (1.1), $\Omega$ is a bounded domain in $\mathbb{R}^2$ and $f(x,y)$ is the *permittivity profile*, defined in terms of the dielectric permittivity $\varepsilon_2(x,y)$ of the membrane, by

$$f(x,y) = \frac{\varepsilon_0}{\varepsilon_2(x,y)}\,. \tag{1.3}$$

This initial condition in (1.1) assumes that the membrane is initially undeflected and that the voltage is applied at time $t = 0$. Mathematically, the pull-in voltage is obtained from (1.2) in terms of the largest possible saddle-node bifurcation value $\lambda_*$ of $\lambda$ for which (1.1) has a steady-state solution.

In the actual design of a MEMS device there are several issues that must be considered. Typically, one of the primary device design goals is to achieve the maximum possible stable steady-state deflection, referred to as the *pull-*

*in distance*, with a relatively small applied voltage $V$. Another consideration may be to increase the stable operating range of the device by increasing the pull-in voltage $V_*$ subject to the constraint that the range of the applied voltage is limited by the available power supply. This increase in the stable operating range may be important for the design of microresonators. For other devices such as microvalves, where touchdown behavior is explicitly exploited, it is of interest to decrease the time for touchdown, thereby increasing the switching speed. One way of achieving larger values of $\lambda_*$, and hence larger values of $V_*$, while simulataneously increasing the pull-in distance, is to use a voltage control scheme imposed by an external circuit in which the device is placed (cf. [**12**]). This approach leads to a nonlocal problem for the deflection of the membrane (cf. [**12**]). A different approach, studied theoretically in [**14**], is to introduce a spatial variation in the dielectric permittivity $\varepsilon_2(x,y)$ of the membrane so that $\varepsilon_2(x,y)$ is largest, and consequently $f(x,y)$ smallest, in the region where the membrane deflection would normally be largest under a spatially uniform permittivity. For a power-law permittivity profile in a slab domain, this approach was shown in [**14**] to allow for an increase in both the pull-in voltage and the pull-in distance.

The first main goal of this paper is to extend the steady-state analysis in [**14**] by giving analytical and numerical results for the saddle-node value $\lambda_*$ and the pull-in distance for (1.1) for some general classes of permittivity profiles $f(x,y)$. For the first class, we assume that $f(x,y)$ is bounded away from zero, so that

$$0 < C_0 \le f(x,y) \le 1\,, \qquad x \in \Omega\,. \tag{1.4}$$

For the second class of profile, we allow for part of the membrane to be perfectly conducting, so that

$$0 \le f(x,y) \le 1\,, \qquad x \in \Omega\,. \tag{1.5}$$

In Theorem 3.1 of [**14**], restated below in Theorem 2.1 of §2, an upper bound for $\lambda_*$ is obtained for permittivity profiles satisfying (1.4). This bound, however, does not apply to profiles satisfying (1.5). In particular, it does not apply to the power-law permittivity profiles considered in §4 of [**14**], which vanish at one point in $\Omega$. To treat this case, in Theorem 2.2 of §2 we use a different approach to obtain an upper bound for $\lambda_*$ for permittivity profiles satisfying (1.5). In §2.1 we give numerical results for $\lambda_*$ for a power-law permittivity profile and an exponential permittivity profile, which satisfy (1.5) and (1.4), respectively. The precise forms for these profiles, which each depend on a parameter $\alpha$, are given below in (2.16). Numerical results for $\lambda_*$ and the pull-in distance as a function of $\alpha$ are given for a slab domain, a unit disk, and a square domain. For large values of $\alpha$, these profiles are such that $f(x,y) \ll 1$ except in a boundary layer near $\partial\Omega$. In this limit, we derive a scaling law for $\lambda*$.

The second main goal of this paper is to analyze and compute time-dependent touchdown behavior for (1.1) for permittivity profiles satisfying either (1.4) or (1.5). The solution $u$ of (1.1) is said to touchdown at finite time if the minimum value of $u$ reaches $-1$ at some $t = T_* < \infty$. At such a time, the membrane touches the bottom fixed plate. In §3.1 we determine bounds on $\lambda$ for which touchdown occurs in finite time. This approach also yields bounds on the touchdown time $T_*$. The first bound, which is obtained from the method of [**6**] (see also [**16**]), applies to a permittivity profile satisfying (1.4). The second bound applies to a permittivity profile satisfying (1.5).

In §3.2 we analytically construct the local touchdown profile for the constant permittivity profile $f(x,y) \equiv 1$. To do so, we introduce a nonlinear change of variables in a similar manner as was used in [**8**] to determine the local behavior of the solution to a semilinear heat equation near the blow-up time and blow-up location. This approach leads to a PDE that has smooth solutions near the touchdown point. By constructing a formal power series solution for this PDE, the local form of the touchdown profile is obtained. As discussed in [**8**], this transformed PDE is also readily amenable to numerical computations. In this way, touchdown behavior is computed numerically. In §3.3, we briefly construct the local touchdown profile for the constant permittivity profile $f(x, y) \equiv 1$ by using a formal center manifold analysis of a PDE that results from a near-similarity group transformation of (1.1). Such a dynamical systems approach has been used previously in [**5**] to study quenching behavior in one space dimension and in [**4**] to study blow-up behavior for a semilinear heat equation in $N$-space dimensions.

In §4 we give some asymptotic results for the touchdown profile for spatially variable permittivity profiles. Numerical results of touchdown behavior are also shown. Finally, in §5, we list a few open mathematical problems.

## 2 The Pull-In Voltage: Location of a Saddle-Node Value

In this section we study the steady-state deflection $u$, which satisfies

$$\Delta u = \frac{\lambda f(x)}{(1+u)^2}\,, \quad x \in \Omega\,; \qquad u = 0\,, \quad x \in \partial\Omega\,; \qquad u > -1\,. \tag{2.1}$$

Here we let $x = (x, y)$ and $\Omega \in \mathbb{R}^2$ is a bounded domain. For several domains shapes $\Omega$ and permittivity profiles $f$, we compute the maximum value of $\lambda$, labeled by $\lambda_*$, for which (2.1) has a solution. This then determines the pull-in voltage from (1.2). Bounds for $\lambda_*$ are also obtained. The bounds on $\lambda_*$ derived below are characterized in terms of the smallest eigenvalue $\mu_0 > 0$, with corresponding eigenfunction $\phi_0$, of the Dirichlet eigenvalue problem

$$\Delta\phi + \mu\phi = 0\,, \quad x \in \Omega\,; \qquad \phi = 0\,, \quad x \in \partial\Omega\,. \tag{2.2}$$

The following result for $\lambda_*$ was proved in [**14**]:

**Theorem 2.1**: *Suppose that $f(x)$ satisfies*

$$0 < C_0 \le f(x) \le 1\,, \quad x \in \Omega\,. \tag{2.3}$$

*Then, there exists a $\lambda_* < \infty$ such that there is no solution to (2.1) for $\lambda > \lambda_*$. Moreover, we have the bound*

$$\lambda_* \le \bar{\lambda}_1 \equiv \frac{4\mu_0}{27 C_0}\,. \tag{2.4}$$

**Proof:** This is Theorem 3.1 of [**14**]. We only briefly sketch the proof here. We fix the sign $\phi_0 > 0$ in $\Omega$. We multiply (2.1) by $\phi_0$, integrate the resulting equation over $\Omega$, and use Green's identity to get

$$\int_\Omega \left( \mu_0 u + \frac{\lambda f(x)}{(1+u)^2} \right) \phi_0 \, dx = 0\,. \tag{2.5}$$

Since $f(x) \ge C_0 > 0$ and $\phi_0 > 0$, the equality in (2.5) is impossible when

$$\mu_0 u + \frac{\lambda C_0}{(1+u)^2} > 0\,, \quad \text{for all } u > -1\,. \tag{2.6}$$

Clearly (2.6) holds for $\lambda$ sufficiently large, which proves that $\lambda_*$ is finite. A simple calculation using (2.6) shows that (2.6) holds when $\lambda > \bar{\lambda}_1$, where $\bar{\lambda}_1$ is given in (2.4). ■

As shown below, the bound (2.4) on $\lambda_*$ is rather good for the constant permittivity profile $f(x) \equiv 1$. However, since this bound relies on the minimum of $f(x)$ on $\Omega$, it cannot be used to estimate $\lambda_*$ for the power-law permittivity profile $f(x) = |x|^\alpha$ with $\alpha > 0$ considered in [**14**]. For such a profile, $C_0 = 0$ in (2.3). Therefore, it is desirable to obtain a bound on $\lambda_*$ that depends on more global properties of $f(x)$. Such a bound is given in the next result.

**Theorem 2.2**: *Suppose that $f(x)$ satisfies*

$$0 \le f(x) \le 1\,, \quad x \in \Omega\,, \tag{2.7}$$

*where $f > 0$ on a set of positive measure. Then, for some $\lambda_* < \infty$, there is no solution to (2.1) for $\lambda > \lambda_*$. Moreover, in terms of the eigenfunction $\phi_0$ of (2.2) normalized by $\int_\Omega \phi_0\, dx = 1$, we have the bound*

$$\lambda_* \leq \bar{\lambda}_2 \equiv \frac{\mu_0}{3} \left( \int_\Omega f\phi_0\, dx \right)^{-1} . \tag{2.8}$$

**Proof:** The proof that $\lambda_*$ is finite follows from (2.5). To obtain the bound (2.8), we take $\phi_0 > 0$ and we normalize $\phi_0$ so that $\int_\Omega \phi_0\, dx = 1$. We then multiply (2.1) by $\phi_0(1+u)^2$, and integrate the resulting equation over $\Omega$ to get

$$\int_\Omega \lambda f \phi_0\, dx = \int_\Omega \phi_0 (1+u)^2 \Delta u\, dx\, . \tag{2.9}$$

Using the identity $\nabla \cdot (Hg) = g\nabla \cdot H + H \cdot \nabla g$ for any smooth scalar field $g$ and vector field $H$, together with the Divergence theorem, we calculate

$$\int_\Omega \lambda f\phi_0\, dx = \int_{\partial\Omega} (1+u)^2 \phi_0 \nabla u \cdot \hat{n}\, dS - \int_\Omega \nabla u \cdot \nabla \left[ \phi_0 (1+u)^2 \right]\, dx\, , \tag{2.10}$$

where $\hat{n}$ is the unit outward normal to $\partial\Omega$. Since $\phi_0 = 0$ on $\partial\Omega$, the first term on the right-hand side of (2.10) vanishes. By calculating the second term on the right-hand side of (2.10), and noting that $u > -1$, we estimate

$$\int_\Omega \lambda f\phi_0\, dx = -\int_\Omega 2(1+u)\phi_0 |\nabla u|^2\, dx - \int_\Omega (1+u)^2 \nabla u \cdot \nabla \phi_0\, dx\, , \tag{2.11 a}$$

$$\leq -\int_\Omega \frac{1}{3} \nabla\phi_0 \cdot \nabla \left[ (1+u)^3 \right]\, dx\, . \tag{2.11 b}$$

The right-hand side of (2.11 *b*) is evaluated explicitly, with the result

$$\int_\Omega \lambda f\phi_0\, dx \leq -\frac{1}{3} \int_{\partial\Omega} (1+u)^3 \nabla\phi_0 \cdot \hat{n}\, dS - \frac{\mu_0}{3} \int_\Omega (1+u)^3 \phi_0\, dx\, . \tag{2.12}$$

For $u > -1$, the last term on the right-hand side of (2.12) is positive. Moreover, $u = 0$ on $\partial\Omega$, and from (2.2) we get that $\int_{\partial\Omega} \nabla\phi_0 \cdot \hat{n}\, dS = -\mu_0$ since $\int_\Omega \phi_0\, dx = 1$. Therefore, if (2.1) has a solution, then, from (2.12), we must have that

$$\lambda \int_\Omega f\phi_0\, dx \leq \frac{\mu_0}{3}\, . \tag{2.13}$$

This proves that there is no solution to (2.1) for $\lambda > \bar{\lambda}_2$, where $\bar{\lambda}_2$ is given in (2.8). ■

### 2.1 Some Explicit Examples

We now compute $\lambda_*$ numerically for several choices of the domain $\Omega$ and the permittivity profile $f(x)$. In the computations below we consider three choices for $\Omega$,

$$\Omega : [-1/2, 1/2] \quad (\text{Slab})\, ; \quad \Omega : x^2 + y^2 \leq 1 \quad (\text{Unit Disk})\, ; \quad \Omega : [0, \sqrt{\pi}] \times [0, \sqrt{\pi}] \quad (\text{Square})\, . \tag{2.14}$$

The unit disk and the square are chosen to have the same area. To compute the bounds $\bar{\lambda}_1$ and $\bar{\lambda}_2$, we must calculate the first eigenpair $\mu_0$ and $\phi_0$ of (2.2), normalized by $\int_\Omega \phi_0\, dx = 1$. A simple calculation yields that

$$\mu_0 = \pi^2\, , \qquad \phi_0 = \frac{\pi}{2} \sin\left[ \pi \left( x + \frac{1}{2} \right) \right]\, , \quad (\text{Slab})\, , \tag{2.15 a}$$

$$\mu_0 = z_0^2 \approx 5.783\, , \qquad \phi_0 = \frac{z_0}{J_1(z_0)} J_0(z_0|x|)\, , \quad (\text{Unit Disk})\, , \tag{2.15 b}$$

$$\mu_0 = 2\pi\, , \qquad \phi_0 = \frac{\pi}{4} \sin\left( \sqrt{\pi} x \right) \sin\left( \sqrt{\pi} y \right)\, , \quad (\text{Square})\, . \tag{2.15 c}$$

[htb]

| $\Omega$ | $\lambda_*$ | $\bar{\lambda}_1$ | $\bar{\lambda}_2$ |
|---|---|---|---|
| (Slab) | 1.401 | 1.462 | 3.290 |
| (Unit Disk) | 0.789 | 0.857 | 1.928 |
| (Square) | 0.857 | 0.931 | 2.094 |

Table 1. Numerical results for the maximum value $\lambda_*$ of $\lambda$ for which (2.1) has a solution for the three domains of (2.14). The upper bounds $\bar{\lambda}_1$ and $\bar{\lambda}_2$ on $\lambda_*$ given in (2.4) and (2.8) are also shown.

Here $J_0$ and $J_1$ are Bessel functions, and $z_0 \approx 2.4048$ is the first zero of $J_0(z)$. The bounds $\bar{\lambda}_1$ and $\bar{\lambda}_2$ are obtained by substituting (2.15) into (2.4) and (2.8). However, $\bar{\lambda}_2$ must typically be evaluated by a numerical quadrature.

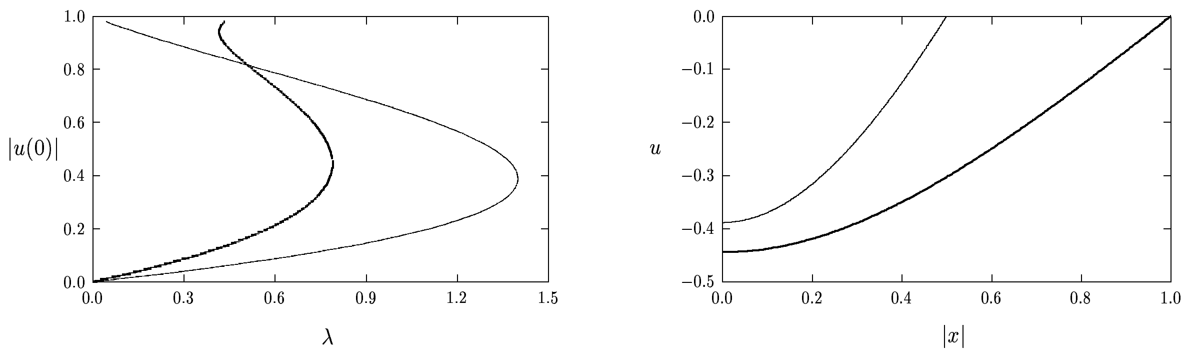


(a) $|u(0)|$ versus $\lambda$ (b) $u$ versus $|x|$

Figure 2. Left figure: plot of $|u(0)|$ versus $\lambda$ for the unit disk (heavy solid curve) and for the slab (solid curve). Right figure: plot of $u$ versus $|x|$ at $\lambda = \lambda_*$ for the unit disk (heavy solid curve) and the slab (solid curve). For both figures we have taken the constant permittivity profile $f \equiv 1$.

We first consider the constant permittivity profile $f(x) \equiv 1$. For the slab domain, the solution to (2.1) can be reduced to quadrature, and $\lambda_*$ can be computed from a transcendental equation. To compute $\lambda_*$ for the unit disk, the scale invariance property of (2.1) can be used as in [**11**] to reduce the boundary value problem (2.1) to an initial value problem, which is then readily solved. Our method for determining $\lambda_*$ for the disk and the slab uses the BVP solver COLSYS (cf. [**1**]) with a Newton iteration step to locate $\lambda_*$. This approach is similar to that employed in [**18**] for Arrhenius nonlinearities and is useful for computing $\lambda_*$ below for spatially varying permittivity profiles. For the square domain, we compute $\lambda_*$ using the nonlinear elliptic solver PLTMG (cf. [**2**]), which uses a finite-element discretization of (2.1) together with path-following methods to compute the solution as $\lambda$ is varied. This software package allows for the accurate computation of saddle-node bifurcation points. In Table 1 we give numerical results for $\lambda_*$ for the three domains of (2.14) together with numerical values for the bounds $\bar{\lambda}_1$ and $\bar{\lambda}_2$. Notice that the bound for $\bar{\lambda}_1$ is rather close to $\lambda_*$, and is better than that of $\bar{\lambda}_2$. In Fig. 2(a) we plot the bifurcation diagram $|u(0)|$ versus $\lambda$ for the slab domain and for the unit disk. For $\lambda = \lambda_*$, in Fig. 2(b) we plot $u$ versus $|x|$ for the slab domain and for the unit disk. In Fig. 3(a) we plot the bifurcation diagram for the square domain. For this domain, in Fig. 3(b) we show a surface plot of $u$ versus $(x, y)$ when $\lambda = \lambda_*$. The computations were done with 1152 finite elements.

For each of the domains of (2.14), we now calculate $\lambda_*$ for the following two forms of the permittivity profile $f(x)$:

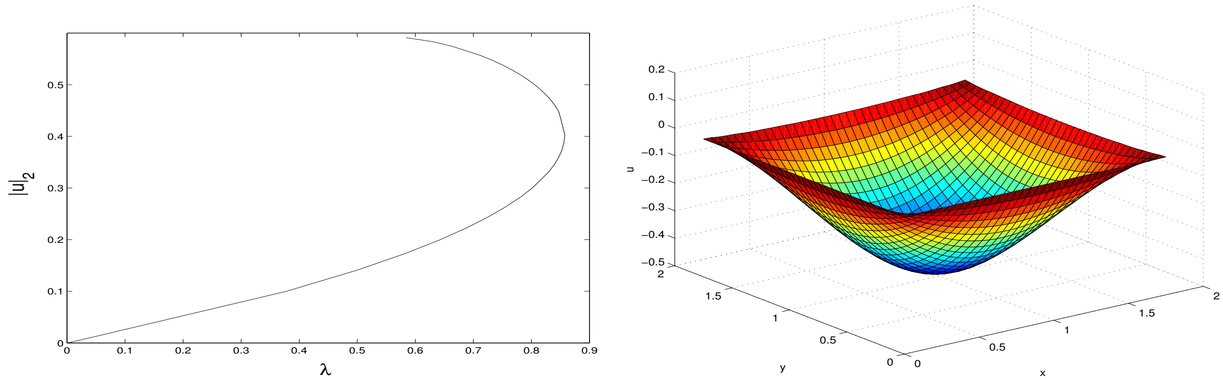


(a) $|u|_2$ versus $\lambda$

(b) $u$ versus $(x, y)$ at $\lambda = \lambda_*$

FIGURE 3. Left figure: plot of the bifurcation diagram of the $L_2$ norm $|u|_2$ versus $\lambda$ for a square domain. We do not show any secondary bifurcations. Right figure: surface plot of $u$ versus $x = (x, y)$ when $\lambda = \lambda_* \approx .857$. For these figures the permittivity profile is $f(x) \equiv 1$.

$$\text{(Slab)}: \quad f(x) = |2x|^{\alpha}, \quad \text{(power-law)}; \quad f(x) = e^{\alpha(x^2 - 1/4)} \quad \text{(exponential)}, \tag{2.16 a}$$

$$\text{(Unit Disk)}: \quad f(x) = |x|^{\alpha}, \quad \text{(power-law)}; \quad f(x) = e^{\alpha(|x|^2 - 1)}, \quad \text{(exponential)}, \tag{2.16 b}$$

$$\text{(Square)}: \quad f(x) = \left(\frac{2}{\pi}\right)^{\alpha/2} |x - x_0|^{\alpha}, \quad \text{(power-law)}; \quad f(x) = \exp\left(\alpha\left(\frac{2|x - x_0|^2}{\pi} - 1\right)\right), \tag{2.16 c}$$

where $\alpha > 0$. In (2.16 $b$) and (2.16 $c$), $x \equiv (x, y)$ and $x_0 = (\sqrt{\pi}/2, \sqrt{\pi}/2)$ is the center of the square. For the domains of (2.14), we note that $0 \leq f(x) \leq 1$ for $x \in \Omega$. In addition, both the power-law and exponential profiles satisfy the property that the minimum of $f(x)$ occurs at the point where the deflection $u$ of the upper membrane in Fig. 1 is the largest. This effect leads to larger values of $\lambda_*$ and, from (1.2), it increases the pull-in voltage. Physically, from (1.3), this corresponds to tailoring the dielectric permittivity $\varepsilon_2$ of the upper membrane so that $\varepsilon_2$ is significantly larger than the free-space permittivity $\varepsilon_0$ in regions where the membrane deflection will be largest. This idea of modifying the dielectric permittivity $\varepsilon_2$ to increase both $\lambda_*$ and the pull-in distance was first introduced and studied in [**14**] for the slab and disk domains. For these domains, it was shown in [**14**] that (2.1) has a scaling invariance property under a power-law profile for $f(x)$. This property, which reduces (2.1) to the study of an ordinary differential equation, was used in [**14**] to give a detailed analysis of the bifurcation diagram of (2.1) for the slab and disk domains. Although the power-law profile for $f(x)$ is mathematically very convenient as a result of the scale invariance property, it is not so realistic from a modeling perspective in that it predicts an infinite dielectric permittivity $\varepsilon_2$ at the center of the membrane. The exponential profile in (2.16) does not have this artifact of an infinite membrane permittivity.

For four values of $\alpha$, in Fig. 4 we plot the bifurcation diagram $|u(0)|$ versus $\lambda$ for both the power-law and the exponential profiles. The plots are shown for both the slab and the unit disk. The bifurcation diagram of the steady-state problem shown in this figure is typical, in that the transition from existence to non-existence is due to the first fold. A more detailed study of the bifurcation diagram for a slab geometry under a power-law profile was made in [**14**]. In [**14**] it was shown that for $0 \leq \alpha < \alpha_c$, where $\alpha_c \equiv -\frac{1}{2} + \frac{1}{2}\sqrt{\frac{27}{2}}$, there is exactly one saddle-node point, and so at most two solutions to (2.1). Alternatively, for $\alpha > \alpha_c$, the bifurcation diagram has an infinite number of fold

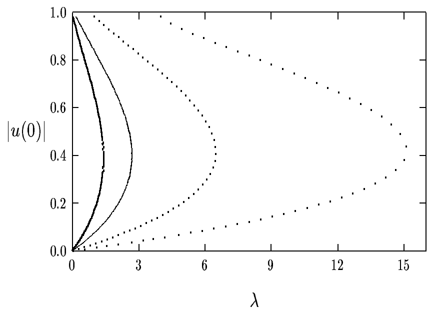


(a) slab, power-law profile

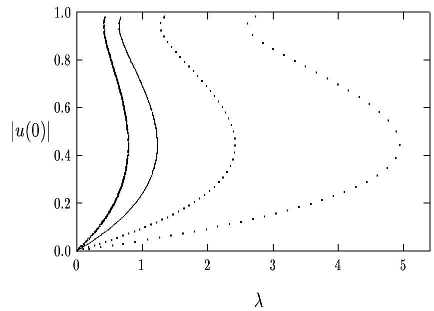


(b) unit disk, power-law profile

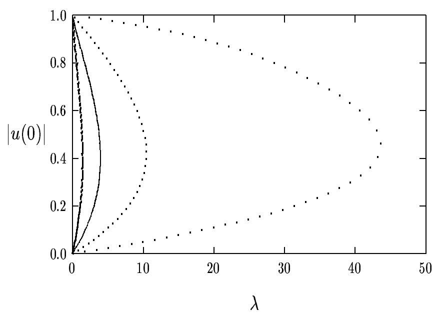


(c) slab, exponential profile

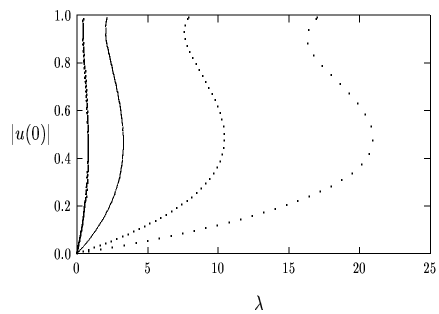


(d) unit disk, exponential profile

FIGURE 4. The bifurcation diagram $|u(0)|$ versus $\lambda$ for the slab and the unit disk, and for both the power-law and exponential profiles. Top left: $\alpha = 0$, $\alpha = 0.5$, $\alpha = 1.5$, $\alpha = 3.0$. Top right: $\alpha = 0$, $\alpha = 0.5$, $\alpha = 1.5$, $\alpha = 3.0$. Bottom left: $\alpha = 0$, $\alpha = 5$, $\alpha = 10$, $\alpha = 19$. Bottom right: $\alpha = 0$, $\alpha = 2$, $\alpha = 4$, $\alpha = 5.6$. In each figure the first saddle-node value increases with $\alpha$.

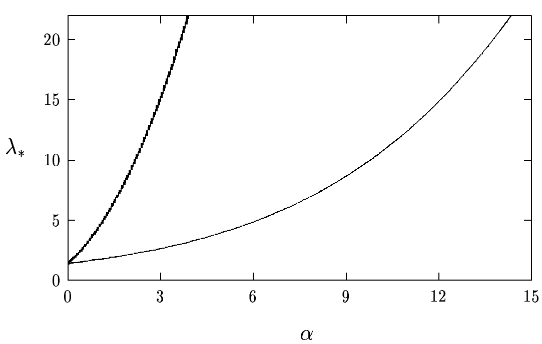


(a) $\lambda_*$ versus $\alpha$ (slab)

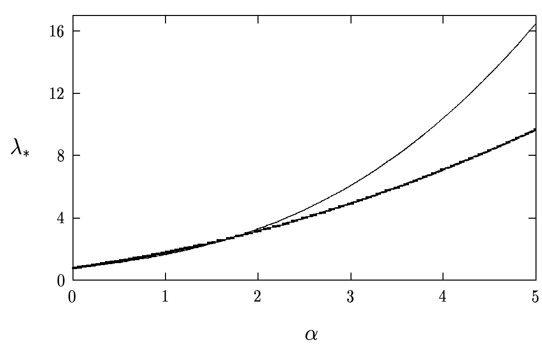


(b) $\lambda_*$ versus $\alpha$ (unit disk)

FIGURE 5. Plots of $\lambda_*$ versus $\alpha$ for a power-law profile (heavy solid curve) and the exponential profile (solid curve). The left figure corresponds to the slab domain, while the right figure corresponds to the unit disk.

[htb]

| $\Omega$ | $\alpha$ | $\lambda_*$ | $\bar{\lambda}_1$ | $\bar{\lambda}_2$ |
|---|---|---|---|---|
| (Slab) | 1.0 | 1.733 | 1.878 | 4.023 |
| (Slab) | 3.0 | 2.637 | 3.095 | 5.965 |
| (Slab) | 6.0 | 4.848 | 6.553 | 10.50 |
| (Slab) | 10.0 | 10.40 | 17.81 | 21.14 |
| (Unit Disk) | 0.5 | 1.153 | 1.413 | 2.706 |
| (Unit Disk) | 1.0 | 1.661 | 2.329 | 3.746 |
| (Unit Disk) | 2.0 | 3.296 | 6.331 | 6.864 |
| (Unit Disk) | 3.0 | 6.091 | 17.21 | 11.86 |

Table 2. Comparison of numerical values for $\lambda_*$ with the bounds $\bar{\lambda}_1$ and $\bar{\lambda}_2$ given in (2.4) and (2.8) for the exponential permittivity profile.

points, which tend to a common limiting value $\lambda_{*c}$ as $u(0) \to -1^+$. Although the details of the solution multiplicity obtained in [**14**] are very interesting, they are not germane to the determination of $\lambda_*$.

In Fig. 5(a) we plot the saddle-node value $\lambda_*$ versus $\alpha$ for the slab domain. A similar plot is shown in Fig. 5(b) for the unit disk. The numerical computations were done using COLSYS [**1**] to solve the boundary value problem (2.1) and Newton's method to determine the saddle-node point. Although Theorem 2.2 guarantees a pull-in voltage for any $\alpha > 0$, $\lambda_*$ is seen to increase rapidly with $\alpha$. Therefore, by increasing $\alpha$, or equivalently by increasing the spatial extent where $f(x) \ll 1$, one can increase the stable operating range of the MEMS capacitor. In Table 2 we give numerical results for $\lambda_*$ together with the bounds $\bar{\lambda}_1$ and $\bar{\lambda}_2$ for the exponential permittivity profile computed from (2.4), (2.8), (2.15), and (2.16). A numerical quadrature is used to evaluate the integral defining $\bar{\lambda}_2$. From this table, we observe that the bound $\bar{\lambda}_1$ for $\lambda_*$ is better than $\bar{\lambda}_2$ for small values of $\alpha$. However, for $\alpha \gg 1$, we can use Laplace's method on the integral defining $\bar{\lambda}_2$ to obtain for the exponential permittivity profile that

$$\bar{\lambda}_1 = \frac{4b_1^2}{27} e^{c_1 \alpha}, \qquad \bar{\lambda}_2 \sim c_2 \alpha^2 . \tag{2.17}$$

Here $b_1 = \pi^2$, $c_1 = 1/4$, $c_2 = 1/3$ for the slab domain, and $b_1 = z_0^2$, $c_1 = 1$, $c_2 = 4/3$ for the unit disk, where $z_0$ is the first zero of $J_0(z) = 0$. Therefore, for $\alpha \gg 1$, the bound $\bar{\lambda}_2$ is better than $\bar{\lambda}_1$. A similar calculation can be done for the power-law profile. Recall for the power-law profile that $\bar{\lambda}_1$ is undefined. However, by using Laplace's method, we readily obtain for $\alpha \gg 1$ that $\bar{\lambda}_2 \sim \alpha^2/3$ for the unit disk and $\bar{\lambda}_2 \sim 4\alpha^2/3$ for the slab domain.

Next, we compute the pull-in distance for a slab domain for both the power-law and the exponential permittvity profiles. The pull-in distance, defined as the value of $|u(0)|$ at the fold point $\lambda = \lambda_*$, gives the maximum stable steady-state membrane deflection that can be achieved. For the slab domain, in Fig. 6(a) we plot $|u(0)|$ versus $\alpha$ for both the power-law and the exponential conductivity profile. For the power-law profile, the plot of $|u(0)|$ versus $\alpha$ is equivalent to that in Fig. 5.1 of [**14**]. A similar plot of $|u(0)|$ versus $\alpha$ is shown in Fig. 6(b) for the unit disk. For the power-law profile in the unit disk we observe that $|u(0)| \approx 0.444$ for any $\alpha > 0$. Therefore, rather curiously, the power-law profile does not increase the pull-in distance for the unit disk. For the exponential profile we observe from Fig. 6(b) that the pull-in distance is not a monotonic function of $\alpha$. The maximum value occurs at $\alpha \approx 4.8$ where $\lambda_* \approx 15.11$ (see Fig. 5(b)) and $|u(0)| = 0.485$. For $\alpha = 0$, we have $\lambda_* \approx 0.789$ and $|u(0)| = 0.444$. Therefore, since $\lambda_*$ is proportional to $V^2$ from (1.2) we conclude that the exponential permittivity profile for the unit disk can increase the pull-in distance by roughly 9% if the voltage is increased by roughly a factor of four.

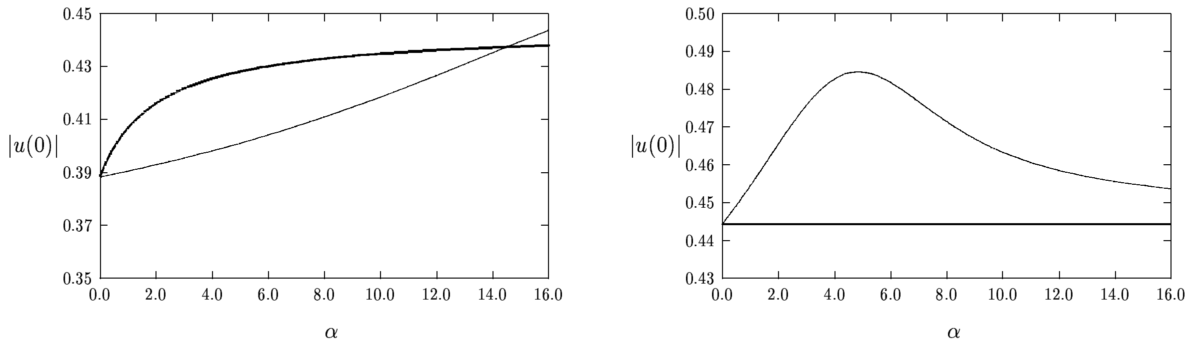


(a) slab

(b) unit disk

FIGURE 6. Plots of the pull-in distance $|u(0)|$ versus $\alpha$ for the power-law profile (heavy solid curve) and the exponential profile (solid curve). Left figure: the slab domain. Right figure: the unit disk.

For device design purposes one of the primary goals is to maximize the pull-in distance over a certain allowable voltage range that is set by the power supply. To address this problem it would be interesting to formulate an optimization problem that computes a dielectric permittivity $f(x)$ that maximizes the pull-in distance for a prescribed range of the saddle-node threshold $\lambda_*$. However, such an optimization problem is beyond the scope of this study.

For the unit disk, in Fig. 7(a) we plot $u$ versus $|x|$ at $\lambda = \lambda_*$ for four values of $\alpha$ for the power-law profile. Notice that $u(0)$ is the same for each of these values of $\alpha$. A similar plot is shown in Fig. 7(b) for the exponential permittivity profile. From these figures, we observe that $u$ has a boundary-layer structure when $\alpha \gg 1$. In this limit, $f(x) \ll 1$ except in a narrow zone near the boundary of the domain. For $\alpha \gg 1$ the pull-in distance $|u(0)|$ also reaches some limiting value (see Fig. 6(a) and Fig. 6(b) and Fig. 7). For the slab domain with an exponential permittivity profile, we remark that the limiting asymptotic behavior of $|u(0)|$ for $\alpha \gg 1$ is beyond the range shown in Fig. 6(a).

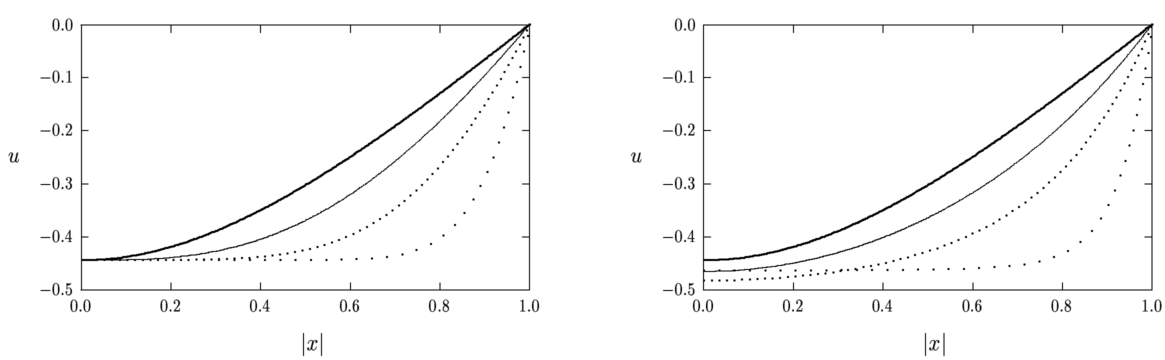


(a) power-law profile

(b) exponential profile

FIGURE 7. Left figure: plots of $u$ versus $|x|$ at $\lambda = \lambda_*$ for $\alpha = 0$, $\alpha = 1$, $\alpha = 3$, and $\alpha = 10$, in the unit disk for the power-law profile. Right figure: plots of $u$ versus $|x|$ at $\lambda = \lambda_*$ for $\alpha = 0$, $\alpha = 2$, $\alpha = 4$, and $\alpha = 10$, in the unit disk for the exponential profile. In both figures the solution develops a boundary-layer structure near $|x| = 1$ as $\alpha$ is increased.

For $\alpha \gg 1$, we now use a boundary-layer analysis to determine a scaling law for $\lambda_*$ for both types of permittivity profiles and for either a slab domain or the unit disk. We illustrate the analysis for a power-law permittivity profile in the unit disk. For $\alpha \gg 1$, there is an outer region defined by $0 \leq r \ll 1 - O(\alpha^{-1})$, and an inner region where $r - 1 = O(1/\alpha)$. In the outer region, where $\lambda r^\alpha \ll 1$, (2.1) reduces asymptotically to $\Delta u = 0$. Therefore, the leading-order outer solution is a constant $u = A$. In the inner region, we introduce new variables $w$ and $\rho$ by

$$w(\rho) = u\,(1 - \rho/\alpha)\,, \qquad \rho = \alpha(1 - r)\,. \tag{2.18}$$

Substituting (2.18) into (2.1) with $f(r) = r^\alpha$, using the limiting behavior $(1 - \rho/\alpha)^\alpha \to e^{-\rho}$ as $\alpha \to \infty$, and defining $\lambda = \alpha^2 \lambda_0$, we obtain the leading-order boundary-layer problem

$$w^{''} = \frac{\lambda_0 e^{-\rho}}{(1+w)^2}\,, \quad 0 \leq \rho < \infty\,; \quad w(0) = 0\,, \quad w^{'}(\infty) = 0\,, \qquad \lambda = \alpha^2 \lambda_0\,. \tag{2.19}$$

In terms of the solution to (2.19), the leading-order outer solution is $u = A = w(\infty)$.

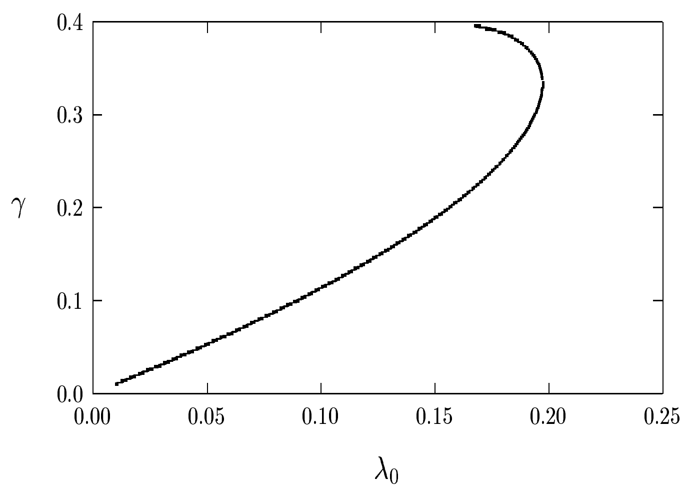


FIGURE 8. Bifurcation diagram of $w^{'}(0) = -\gamma$ versus $\lambda_0$ from the numerical solution of (2.19).

We define $\gamma$ by $w^{'}(0) = -\gamma$, for $\gamma > 0$, and we solve (2.19) numerically using COLSYS [**1**] to determine $\lambda_0 = \lambda_0(\gamma)$. In Fig. 8 we plot $\lambda_0(\gamma)$ and show that this curve has a saddle-node point at $\lambda_0 = \lambda_{0*} \equiv 0.1973$. At this value, we compute $w(\infty) \approx 0.445$, which sets the limiting membrane deflection for $\alpha \gg 1$. Therefore, for $\alpha \gg 1$, the saddle-node value, from (2.19), has the scaling law behavior $\lambda_* \sim 0.1973\alpha^2$ for a power-law profile in the unit disk. A similar boundary-layer analysis can be done to determine the scaling law for $\lambda_*$ when $\alpha \gg 1$ for the other cases. In each case we can relate $\lambda_*$ to the saddle-node value of the boundary-layer problem (2.19). In this way, for $\alpha \gg 1$, we obtain

$$\lambda_* \sim 4(0.1973)\alpha^2\,, \quad \bar{\lambda}_2 \sim \frac{4\alpha^2}{3}\,, \quad \text{(power-law, slab), (exponential, unit disk)}\,, \tag{2.20 a}$$

$$\lambda_* \sim (0.1973)\alpha^2\,, \quad \bar{\lambda}_2 \sim \frac{\alpha^2}{3}\,, \quad \text{(power-law, unit disk), (exponential, slab)}\,, \tag{2.20 b}$$

Notice that $\bar{\lambda}_2 = O(\alpha^2)$, with a factor that is about $5/3$ times as large as the multiplier of $\alpha^2$ in the asymptotic formula for $\lambda_*$. For an exponential profile and a power-law profile in the unit disk, in Fig. 9(a) and Fig. 9(b), respectively, we show the close agreement between the full numerical value of $\lambda_*$ and the asymptotic result (2.20).

For the square domain we use PLTMG (cf. [**2**]) to compute $\lambda_*$ as a function of $\alpha$. In Fig. 10(a) we plot $\lambda_*$ versus

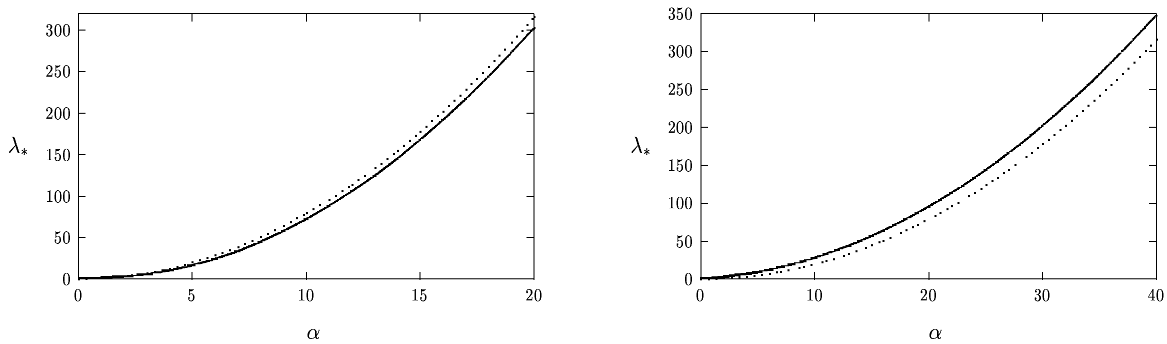


(a) exponential profile (b) power law profile

FIGURE 9. Comparison of numerically computed $\lambda_*$ (heavy solid curve) with the asymptotic result (dotted curve) from (2.20) for the unit disk. Left figure: the exponential profile. Right figure: the power-law profile.

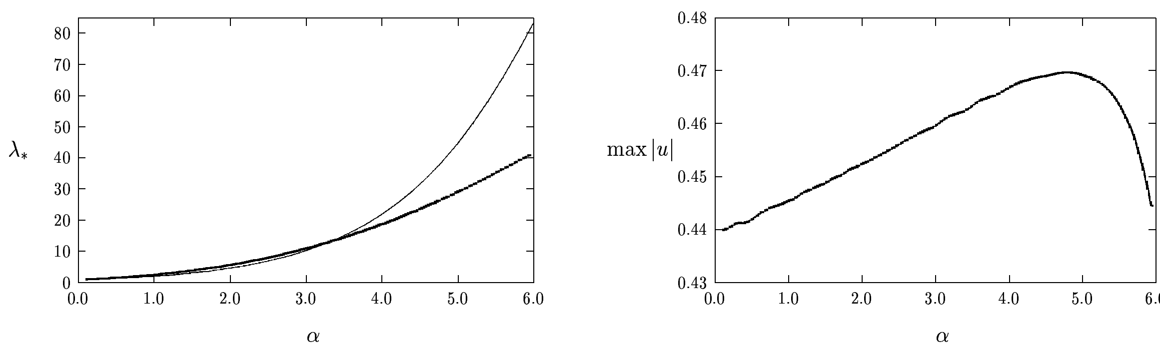


(a) $\lambda_*$ (b) $\max|u|$

FIGURE 10. Left figure: $\lambda_*$ versus $\alpha$ for the square domain. The power-law profile is the heavy solid curve and the exponential profile is the solid curve. Right figure: the pull-in distance $\max|u|$ at $\lambda = \lambda_*$ versus $\alpha$ for the exponential profile in the square domain.

[htb]

| $\alpha$ | $\lambda_*$ (power-law) | $\lambda_*$ (exponential) |
|---|---|---|
| 0.5 | 1.523 | 1.314 |
| 1.0 | 2.485 | 2.005 |
| 2.0 | 5.607 | 4.589 |
| 3.0 | 10.85 | 10.21 |
| 4.0 | 18.67 | 21.89 |
| 5.0 | 29.04 | 44.61 |
| 6.0 | 41.67 | 83.31 |
| 7.0 | 56.38 | 132.6 |

Table 3. Numerical results for $\lambda_*$ versus $\alpha$ for the exponential and power-law permittivity profiles of (2.16 $c$). The computations are for the square domain $[0, \sqrt{\pi}] \times [0, \sqrt{\pi}]$.

$\alpha$ for both the power-law and exponential profiles of (2.16 $c$). In Table 3 we give numerical results for $\lambda_*$ at different values of $\alpha$ for both profiles. The computations were done with 3200 finite elements. From this table we observe that $\lambda_*$ increases rapidly with $\alpha$. In Fig. 10(b) we plot the pull-in distance $\max|u|$ versus $\alpha$ at $\lambda = \lambda_*$ for the exponential permittivity profile. This curve has the same qualitative shape as for the case of the unit disk shown in Fig. 6(b). For the values of $\alpha$ shown in Fig. 10(b) the maximum deflection occurs at the center of the square. For the power-law profile our numerical computations (not shown) indicate that, as for the case of the unit disk in Fig. 6(a), the membrane deflection at $\lambda = \lambda_*$ is essentially independent of $\alpha$ provided that $\alpha$ is not too large.

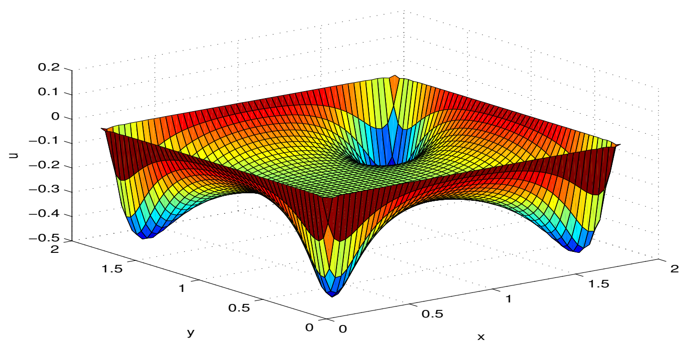


FIGURE 11. Plot of the numerical solution for $u$ in the square domain at the fold point $\lambda_*$ for the exponential permittivity profile with $\alpha = 8$. The maximum deflection now occurs near each of the four corners of the square where the dielectric permittivity function $f$ is the largest.

For $\alpha \gg 1$ the solution $u$ under either a power-law or an exponential dielectric permittivity profile develops strong gradients in the localized regions where $f(x, y) \approx 1$. In contrast to the case of the unit disk where $f \approx 1$ near the boundary $r = 1$, for the square domain we have $f \approx 1$ for $\alpha \gg 1$ only in small neighbourhoods near each of the four corners of the square. Away from these corners we have $f \ll 1$ when $\alpha \gg 1$. In Fig. 11, where we plot the numerical solution for $u$ in the square domain at the fold point $\lambda_*$ for the exponential permittivity profile with $\alpha = 8$, we observe that the maximum deflection now occurs near each of the corners of the square.

## 3 Touchdown behavior

We now study touchdown, or quenching, behavior for (1.1). The solution $u$ of (1.1) is said to touchdown at finite time if the minimum value of $u$ reaches $-1$ at some $t = T_* < \infty$. In §3.1 we determine bounds on $\lambda$ for which touchdown occurs in finite time. In §3.2 we analytically construct the local touchdown profile for the case $f(x) \equiv 1$. For $f(x) \equiv 1$, in §3.3 we briefly outline the construction of the local touchdown profile by using a formal center manifold analysis of a PDE, similar to that in [**5**] and [**4**], that results from a similarity group transformation of (1.1).

### 3.1 Bounds on Touchdown Behavior

Let $\mu_0$ and $\phi_0$ be the smallest eigenpair of (2.2). The first result is a minor modification of a key result in [**6**].

**Theorem 3.1**: *Suppose that $f(x)$ satisfies*

$$0 < C_0 \le f(x) \le 1\,, \quad x \in \Omega\,, \tag{3.1}$$

*and that $\lambda > \bar{\lambda}_1 \equiv \frac{4\mu_0}{27C_0}$. Then, the solution $u$ of (1.1) reaches $u = -1$ at finite time.*

**Proof:** Without loss of generality we assume that $\phi_0 > 0$ in $\Omega$, and we normalize $\phi_0$ so that $\int_\Omega \phi_0\, dx = 1$. Multiplying (1.1) by $\phi_0$, and integrating over the domain, we obtain

$$\frac{d}{dt}\int_\Omega \phi_0 u\, dx = \int_\Omega \phi_0 \Delta u\, dx - \int_\Omega \frac{\lambda \phi_0 f(x)}{(1+u)^2}\, dx\,. \tag{3.2}$$

Using Green's theorem, together with the lower bound in (3.1), we get

$$\frac{d}{dt}\int_\Omega \phi_0 u\, dx \le -\mu_0 \int_\Omega \phi_0 u\, dx - \lambda C_0 \int_\Omega \frac{\phi_0}{(1+u)^2}\, dx\,. \tag{3.3}$$

Next, we define an energy-like variable $E(t)$ by $E(t) = \int_\Omega \phi_0 u\, dx$, where $E(0) = 0$, so that

$$E(t) = \int_\Omega \phi_0 u\, dx \ge \inf_\Omega u \int_\Omega \phi_0\, dx = \inf_\Omega u\,. \tag{3.4}$$

Then, using Jensen's inequality on the second term on the right-hand side of (3.3), we obtain

$$\frac{dE}{dt} + \mu_0 E \le -\frac{\lambda C_0}{(1+E)^2}\,, \qquad E(0) = 0\,. \tag{3.5}$$

We then compare $E(t)$ with the solution $F(t)$ of

$$\frac{dF}{dt} + \mu_0 F = -\frac{\lambda C_0}{(1+F)^2}\,, \qquad F(0) = 0\,. \tag{3.6}$$

It then follows from standard comparison principles that $E(t) \le F(t)$ on their domains of existence. Therefore,

$$\inf_\Omega u \le E(t) \le F(t)\,. \tag{3.7}$$

Next, we separate variables in (3.6) to determine $t$ in terms of $F$. The touchdown time $T_1$ for $F$ is obtained by setting $F = -1$ in the resulting formula. In this way, we get

$$T_1 \equiv \int_{-1}^{0} \left[\mu_0 s + \frac{\lambda C_0}{(1+s)^2}\right]^{-1} ds\,. \tag{3.8}$$

The touchdown time $T_1$ is finite when the integral in (3.8) converges. A simple calculation shows that this occurs when $\lambda > \bar\lambda_1 \equiv \frac{4\mu_0}{27C_0}$. Hence if $T_1$ is finite, then (3.7) implies that the touchdown time $T_*$ of (1.1) must also be finite. Therefore, when $\lambda > \bar\lambda_1 = \frac{4\mu_0}{27C_0}$, we have that $T_* < T_1$, where $T_1$ is given in (3.8) . ■

Recalling Theorem 3.1 in [**14**], which was summarized in Theorem 2.1 of §2, we conclude that not only is there no steady-state solution for (1.1) when $\lambda > \bar\lambda_1$, but the corresponding time-dependent solution of (1.1) touches down in finite time. We are not able to obtain any theoretical information on touchdown behavior for the range $\lambda_* < \lambda < \bar\lambda_1$. Tne next result, using the approach of Theorem 2.2 of §2, establishes touchdown behavior for more general permittivity profiles $f(x)$, such as the power-law profile, that vanish at certain points in $\Omega$.

**Theorem 3.2**: *Suppose that $f$ satisfies (2.7), and that $\lambda > \bar\lambda_2$, where $\bar\lambda_2$ is defined in (2.8). Then, the solution $u$ of (1.1) reaches $-1$ at finite time.*

**Proof:** Let $\phi_0$ and $\mu_0$ be the smallest eigenpair of (2.2). We fix the sign $\phi_0 > 0$ in $\Omega$, and we normalize $\phi_0$ so that $\int_\Omega \phi_0\, dx = 1$. We multiply (1.1) by $\phi_0(1+u)^2$, and integrate the resulting equation over $\Omega$ to get

$$\frac{d}{dt}\int_\Omega \frac{\phi_0}{3}(1+u)^3\, dx = \int_\Omega \phi_0 (1+u)^2 \Delta u\, dx - \int_\Omega \lambda f \phi_0\, dx\,. \tag{3.9}$$

We calculate the first term on the right-hand side of (3.9) as in the proof of Theorem 2.2 to get

$$\frac{d}{dt}\int_\Omega \frac{\phi_0}{3}(1+u)^3\,dx = -\int_\Omega \nabla u\cdot\nabla\left[\phi_0(1+u)^2\right]\,dx - \int_\Omega \lambda f\phi_0\,dx\,, \tag{3.10 a}$$

$$= -\int_\Omega 2(1+u)\phi_0|\nabla u|^2\,dx - \int_\Omega \frac{1}{3}\nabla\phi_0\cdot\nabla\left[(1+u)^3\right]\,dx - \int_\Omega \lambda f\phi_0\,dx\,, \tag{3.10 b}$$

$$\le -\frac{1}{3}\int_{\partial\Omega}\nabla\phi_0\cdot\hat{n}\,dS - \frac{\mu_0}{3}\int_\Omega (1+u)^3\phi_0\,dx - \int_\Omega \lambda f\phi_0\,dx\,. \tag{3.10 c}$$

Since $\int_\Omega \nabla\phi_0\cdot\hat{n}\,dS = -\mu_0$, and $u\ge -1$, we further estimate from (3.10 $c$) that

$$\frac{dE}{dt}+\mu_0 E\le R\,,\qquad R\equiv\frac{\mu_0}{3}-\lambda\int_\Omega f\phi_0\,dx\,,\qquad E\equiv\frac{1}{3}\int_\Omega \phi_0(1+u)^3\,dx\,,\qquad . \tag{3.11}$$

Next, we compare $E(t)$, which satisfies $E(0)=1/3$, with the solution $F(t)$ of

$$\frac{dF}{dt}+\mu_0F=R\,,\qquad F(0)=\frac{1}{3}\,. \tag{3.12}$$

By standard comparison principles, and the definition of $E$, we obtain

$$\frac{1}{3}\inf_\Omega (1+u)^3\le E(t)\le F(t)\,. \tag{3.13}$$

Assume that $\lambda>\bar{\lambda}_2$, where $\bar{\lambda}_2$ is defined in (2.8). For this range of $\lambda$, we have that $R<0$ in (3.11) and (3.12). For $R<0$, we have that $F=0$ at some finite time $t=T_2$. From (3.13), this implies that $E=0$ at finite time. Thus, $u$ has touchdown at some finite time $T_*<T_2$. Then, by calculating $T_2$ explicitly, we get the following bound on $T_*$:

$$T_*<T_2\equiv -\frac{1}{\mu_0}\log\left[1-\frac{\mu_0}{3\lambda}\left(\int_\Omega f\phi_0\,dx\right)^{-1}\right]\,. \tag{3.14}$$

The operation of a microvalve in MEMS technology explicitly exploits the existence of touchdown behavior in order to open and close a switch (see §7.6 of [**13**]). The bounds on the touchdown time above relate to the time it takes to open such a valve, and thereby gives an estimate on the switching speed. To estimate the switching speed as a function of $\alpha$, we label $I(\alpha)\equiv\int_\Omega f\phi_0\,dx$. For both the power-law and exponential permittivity profiles we calculate that $I'(\alpha)>0$ and that $I(\alpha)\sim c\alpha^{-2}$ for $\alpha\gg 1$ for some $c>0$. Therefore, from (3.14) we obtain that $T_2$ is an increasing function of $\alpha$ and that $T_2'(\alpha)\sim 2\alpha/(3c\lambda)$ for $\alpha\gg 1$. This suggests that the switching speed decreases as $\alpha$ increases.

### 3.2 The Touchdown Profile $f(x)\equiv 1$: Transformed Problem

We now construct a local expansion of the solution near the touchdown time and touchdown location by adapting the method of [**8**] used to analyze blow-up behavior. In the analysis below we assume that touchdown occurs at $x=0$ and $t=T$. In the absence of diffusion, the time-dependent behavior of (1.1) is given by $u_t=-\lambda(1+u)^{-2}$. Integrating this differential equation and setting $u(T)=-1$, we get $(1+u)^3=-3\lambda(t-T)$. This solution motivates the introduction of a new variable $v(x,t)$ defined in terms of $u(x,t)$ by

$$v=\frac{1}{3\lambda}(1+u)^3\,. \tag{3.15}$$

Notice that $u=-1$ maps to $v=0$. In terms of $v$, (1.1) transforms exactly to

$$v_t=\Delta v-\frac{2}{3v}|\nabla v|^2-1\,,\quad x\in\Omega\,;\qquad v=\frac{1}{3\lambda}\,,\quad x\in\partial\Omega\,;\qquad v=\frac{1}{3\lambda}\,,\quad t=0\,. \tag{3.16}$$

. We will find a formal power series solution to (3.16) near $v = 0$ in dimension $N = 1$ and $N = 2$.

As in [**8**] we look for a locally radially symmetric solution to (3.16) in the form

$$v(x,t) = v_0(t) + \frac{r^2}{2!}v_2(t) + \frac{r^4}{4!}v_4(t) + \cdots\,, \tag{3.17}$$

where $r = |x|$. In dimension $N = 1$, such a form implies that the touchdown profile is locally even. We then substitute (3.17) into (3.16) and collect coefficients in $r$. In this way, we obtain the following coupled ordinary differential equations for $v_0$ and $v_2$:

$$v_0^{'} = -1 + Nv_2\,, \qquad v_2^{'} = -\frac{4}{3v_0}v_2^2 + \frac{(N+2)}{3}v_4\,. \tag{3.18}$$

We are interested in the solution to this system for which $v_0(T) = 0$, with $v_0^{'} < 0$ and $v_2 > 0$ for $T - t > 0$ with $T - t \ll 1$. The system (3.18) has a closure problem in that $v_2$ depends on $v_4$. However, we will assume that $v_4 \ll v_2^2/v_0$ near the singularity. With this assumption, (3.18) reduces to

$$v_0^{'} = -1 + Nv_2\,, \qquad v_2^{'} = -\frac{4}{3v_0}v_2^2\,. \tag{3.19}$$

We now solve the system (3.19) asymptotically as $t \to T^-$ in a similar manner as was done in [**8**]. We first assume that $Nv_2 \ll 1$ near $t = T$. This leads to $v_0 \sim T - t$, and the following differential equation for $v_2$:

$$v_2^{'} \sim \frac{-4}{3(T-t)}v_2^2\,, \quad \text{as } t \to T^-\,. \tag{3.20}$$

By integrating (3.20), we obtain that

$$v_2 \sim -\frac{3}{4\left[\log(T-t)\right]} + \frac{B_0}{\left[\log(T-t)\right]^2} + \cdots\,, \quad \text{as } t \to T^-\,, \tag{3.21}$$

for some unknown constant $B_0$. From (3.21), we observe that the consistency condition that $Nv_2 \ll 1$ as $t \to T^-$ is indeed satisfied. Substituting (3.21) into the equation (3.19) for $v_0$, we obtain for $t \to T^-$ that

$$v_0^{'} = -1 + N\left(-\frac{3}{4\left[\log(T-t)\right]} + \frac{B_0}{\left[\log(T-t)\right]^2} + \cdots\right)\,. \tag{3.22}$$

Using the method of dominant balance, we look for a solution to (3.22) as $t \to T^-$ in the form

$$v_0 \sim (T-t) + (T-t)\left[\frac{C_0}{\left[\log(T-t)\right]} + \frac{C_1}{\left[\log(T-t)\right]^2} + \cdots\right]\,, \tag{3.23}$$

for some $C_0$ and $C_1$ to be found. A simple calculation yields that

$$v_0 \sim (T-t) - \frac{3N(T-t)}{4|\log(T-t)|} - \frac{N\left(B_0 - 3/4\right)(T-t)}{|\log(T-t)|^2} + \cdots\,, \quad \text{as } t \to T^-\,. \tag{3.24}$$

The local form for $v$ near touchdown is $v \sim v_0 + r^2 v_0/2$. Using the leading term in $v_2$ from (3.21) and the first two terms in $v_0$ from (3.24), we obtain the local form

$$v \sim (T-t)\left[1 - \frac{3N}{4|\log(T-t)|} + \frac{3r^2}{8(T-t)|\log(T-t)|} + \cdots\right]\,, \tag{3.25}$$

for $r \ll 1$ and $t - T \ll 1$. Finally, using the nonlinear mapping (3.15) relating $u$ and $v$, we conclude that

$$u \sim -1 + \left[3\lambda(T-t)\right]^{1/3}\left(1 - \frac{3N}{4|\log(T-t)|} + \frac{3r^2}{8(T-t)|\log(T-t)|} + \cdots\right)^{1/3}\,. \tag{3.26}$$

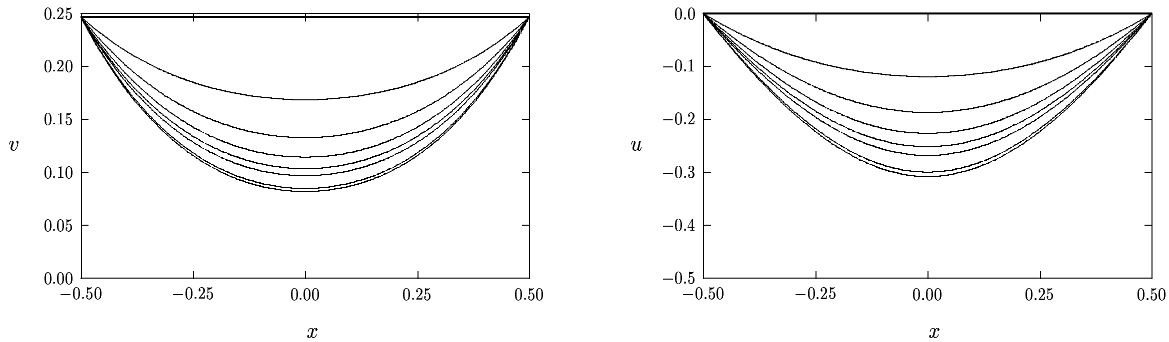


(a) $v$ versus $x$

(b) $u$ versus $x$

FIGURE 12. Experiment 1: for the slab domain and $\lambda = 1.35 < \lambda_*$ we plot $v$ and $u$ versus $x$ at times $t = (0, 0.1, 0.2, 0.3, 0.4, 0.5, 1.0, 3.0)$ from the discrete scheme (3.28) with $N = 200$ and $\Delta t = 0.6 \times 10^{-5}$. Both $v$ and $u$ decrease towards a steady-state solution as $t$ increases.

We note, as in [**8**], that if we use the local behavior $v \sim (T-t) + 3r^2/[8|\log(T-t)|]$, we get that

$$\frac{|\nabla v|^2}{v} \sim \left[\frac{2}{3}|\log(T-t)| + \frac{16(T-t)|\log(T-t)|^2}{9r^2}\right]^{-1} . \tag{3.27}$$

Hence, the term $|\nabla v|^2/v$ in (3.16) is bounded for any $r$, even as $t \to T^-$. This allows us to use a simple finite-difference scheme to compute numerical solutions to (3.16). With this observation, we now perform a few numerical experiments on the transformed problem (3.16). For the slab domain, we define $v_j^m$ for $j = 1, \ldots, N+2$ to be the discrete approximation to $v(m\Delta t, -1/2 + (j-1)h)$, where $h = 1/(N+1)$ and $\Delta t$ are the spatial and temporal mesh sizes, respectively. A second order accurate in space and first order accurate in time discretization of (3.16) is

$$v_j^{m+1} = v_j^m + \Delta t \left( \frac{\left(v_{j+1}^m - 2v_j^m + v_{j-1}^m\right)}{h^2} - 1 - \frac{\left(v_{j+1}^m - v_{j-1}^m\right)^2}{6 v_j^m h^2} \right) , \qquad j = 2, \ldots, N+1 , \tag{3.28}$$

with $v_1^m = v_{N+2}^m = (3\lambda)^{-1}$ for $m \geq 0$. The initial condition is $v_j^0 = (3\lambda)^{-1}$ for $j = 1, \ldots, N+2$. The time-step $\Delta t$ is chosen to satisfy $\Delta t < h^2/4$ for the stability of the discrete scheme.

**Experiment 1:** We consider the slab domain $|x| \leq 1/2$ with $\lambda = 1.35$. We took $\Delta t = 0.60 \times 10^{-5}$ and $N = 200$, so that $h = 0.49751 \times 10^{-2}$. Since $\lambda < \lambda_* \approx 1.401$ from Table 1, we expect that the time-dependent solution will approach the steady-state solution on the lower branch of the $|u(0)|$ versus $\lambda$ bifurcation diagram. This is shown in Fig. 12(a) and Fig. 12(b) where we plot $v$ and $u = -1 + (3\lambda v)^{1/3}$ versus $x$, respectively.

**Experiment 2:** Next, we consider the slab domain with $\lambda = 1.5$. From Table 1 we note that $\bar{\lambda}_2 > \lambda > \bar{\lambda}_1 > \lambda_*$. Therefore, Theorem 3.1 guarantees touchdown in a finite time $T_*$ with $T_* < T_1$, where $T_1 = 2.040$ as computed numerically from (3.8). Since $\lambda < \bar{\lambda}_2$, the bound $T_2$ for the touchdown time, as given in (3.14), is undefined. For the discrete scheme (3.28) we took $\Delta t = 0.60 \times 10^{-5}$ and $N = 200$, so that $h = 0.49751 \times 10^{-2}$. To determine the touchdown time accurately, we took time-steps smaller than this value of $\Delta t$ when the minimum value of $v$ dropped below some small threshold. In this way, we found that touchdown occurs at $x = 0$ and at $T_* \approx 1.07366$. In Fig. 13(a) and Fig. 13(b) we plot $v$ and $u = -1 + (3\lambda v)^{1/3}$ versus $x$, respectively, showing touchdown behavior in finite time.

In Fig. 14(a) we compare the numerical approximation for $v$ with the local behavior (3.25) at $t = 1.0736$. In (3.25)

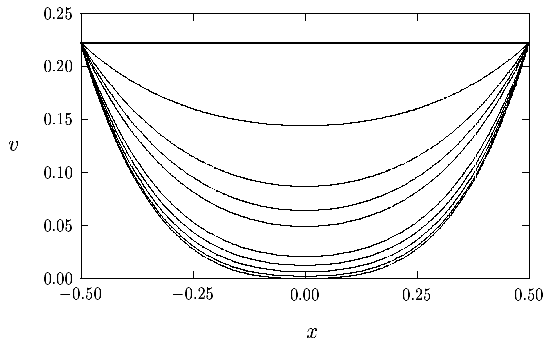


(a) $v$ versus $x$

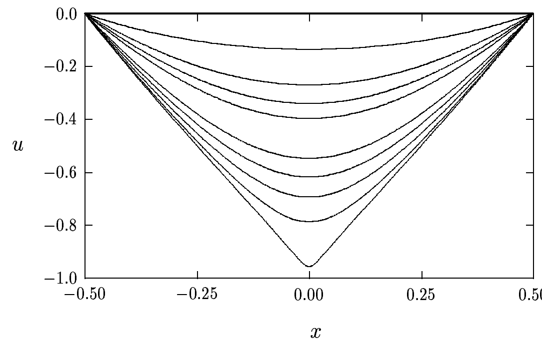


(b) $u$ versus $x$

FIGURE 13. Experiment 2: for the slab domain and $\lambda = 1.5 > \lambda_*$ we plot $v$ and $u$ versus $x$ at times $t = (0, 0.1, 0.3, 0.5, 0.7, 1.0, 1.04, 1.06, 1.07, 1.07364)$ from the discrete scheme (3.28) with $N = 200$, and $\Delta t = 0.6 \times 10^{-5}$. For this data, there is touchdown in finite time.

we set $N = 1$ and use $T = 1.07366$ for the touchdown time. From this figure we observe that the local asymptotic result (3.25) compares favorably with the numerical result. As a remark, if we took a coarser mesh with $N = 150$ meshpoints, so that $h = 0.66225 \times 10^{-2}$, and chose $\Delta t = 0.1 \times 10^{-4}$, then the touchdown time is $T_* \approx 1.07357$.

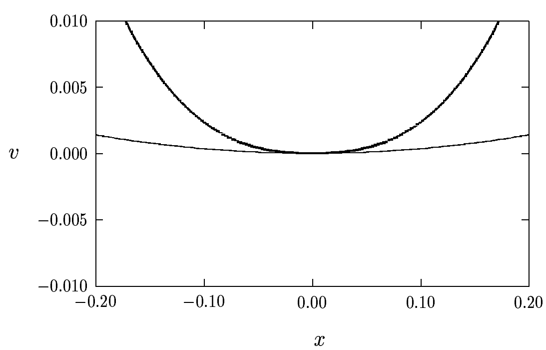


(a) slab domain: $t = 1.0736$

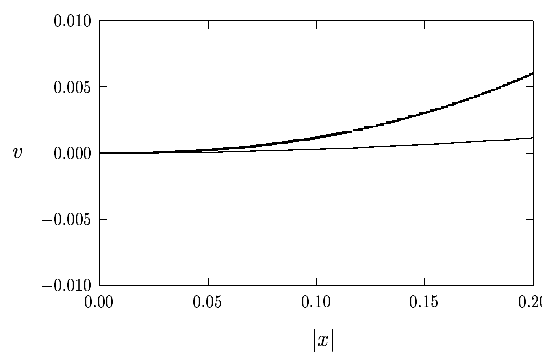


(b) unit disk: $t = 0.7228$

FIGURE 14. Plot of discrete approximation for $v$ (heavy solid curve) and the local approximation for $v$ (solid curve) given in (3.25). Left figure: slab domain with $T = 1.07366$. Right figure: unit disk with $T = 0.722858$.

**Experiment 3:** Next, we consider the unit disk with $f(x) \equiv 1$ and $\lambda = 1.0$. From Table 1 we note that $\bar{\lambda}_2 > \lambda > \bar{\lambda}_1 > \lambda_*$. Therefore, Theorem 3.1 guarantees touchdown in a finite time $T_*$ with $T_* < T_1$, where $T_1 = 1.140$ as computed numerically from (3.8). Since $\lambda < \bar{\lambda}_2$, $T_2$ in (3.14) is undefined. A second order accurate in space and first order accurate in time discrete approximation to (3.16), with spatial meshsize $h$, on $0 \leq r \leq 1$ and $t \geq 0$ is

$$v_j^{m+1} = v_j^m + \Delta t \left( \frac{\left(v_{j+1}^m - 2v_j^m + v_{j-1}^m\right)}{h^2} + \frac{\left(v_{j+1}^m - v_{j-1}^m\right)}{2hr_j} - 1 - \frac{\left(v_{j+1}^m - v_{j-1}^m\right)^2}{6v_j^m h^2} \right), \qquad j = 2, \ldots, N+1, \quad (3.29\,a)$$

where $r_j = jh$. From [**9**] (see page 50), the discrete approximation for $v_1$ at the origin $r = 0$ is

$$v_1^{m+1} = v_1^m + \frac{4\Delta t}{h^2}\left(v_2^m - v_1^m\right) . \tag{3.29 b}$$

The condition at $r = 1$ is $v_{N+2}^m = (3\lambda)^{-1}$. The results shown below are for $\Delta t = 0.6 \times 10^{-5}$ and $N = 200$, so that $h = 0.49751 \times 10^{-2}$. For these values, the touchdown time is found to be $T_* \approx 0.722858$.

In Fig. 15(a) and Fig. 15(b) we plot $v$ and $u = -1 + (3\lambda v)^{1/3}$ versus $x$, respectively, showing touchdown behavior in finite time. In Fig. 14(b) we compare the numerical approximation for $v$ with the local behavior (3.25) at $t = 0.7228$. In (3.25) we set $N = 2$ and use $T = 0.722858$ for the touchdown time.

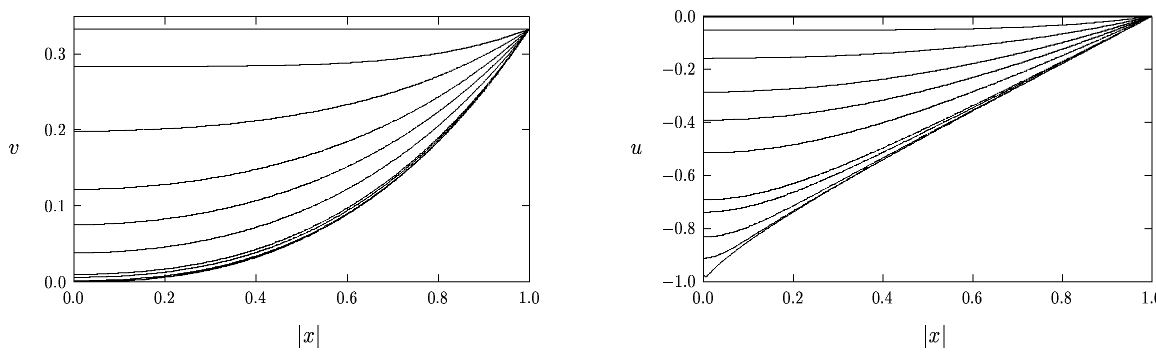


(a) $v$ versus $|x|$ (b) $u$ versus $|x|$

FIGURE 15. Experiment 3: for the unit disk and $\lambda = 1.0$ we plot $v$ and $u$ versus $|x|$ at times $t = (0.05, 0.15, 0.30, 0.45, 0.60, 0.70, 0.71, 0.72, 0.7225, 0.722856)$. For the discrete scheme (3.29) with $N = 200$, and $\Delta t = 0.6 \times 10^{-5}$, we compute the touchdown time $T_* \approx 0.722858$.

**Experiment 4:** Finally, we give an example of touchdown behavior in the square domain $[0, \sqrt{\pi}] \times [0, \sqrt{\pi}]$ for the constant permittivity profile $f(x, y) \equiv 1$ with $\lambda = 2.0$. From Table 1 we note that $\bar{\lambda}_2 > \lambda > \bar{\lambda}_1 > \lambda_* \approx 0.857$. Therefore, Theorem 3.1 guarantees touchdown in a finite time $T_*$ with $T_* < T_1$, where $T_1 = 0.2521$ as computed numerically from (3.8). Since $\lambda < \bar{\lambda}_2$, $T_2$ in (3.14) is undefined.

The discretization of (3.16) is similar to that given in (3.28). We use centered differences in $x$ and $y$ to compute discrete approximations to $v_{xx}$ and $v_{yy}$ for $\Delta v$. Centered differences are then used in $x$ and $y$ to compute $|\nabla v|^2$. An explicit Euler method is then used for the time integration. For a discretization of 150 meshpoints in each of the $x$ and $y$ directions, and with a time-step of $\Delta t = 0.15 \times 10^{-4}$, which is decreased near touchdown, we compute a touchdown time $T_* \approx 0.19751$. Notice that $T_1 = .2521$ is a reasonably good bound on the touchdown time. The touchdown point $(x_0, y_0) = (.880, .880)$ is at the center of the square. In Fig. 16(a) we plot the numerically computed $u$ versus $(x, y)$ for $t = 0.1975$, which is very close to the singularity time. A plot of $v$ versus $(x, y)$ is shown in Fig. 16(b).

### 3.3 The Touchdown Profile $f(x) \equiv 1$: Center Manifold Analysis

A different approach to determine the local touchdown profile when $f(x) \equiv 1$ is based on the center manifold analysis of a PDE that results from a similarity group transformation of (1.1). This approach was used in [**5**] for the case $N = 1$. A closely related method was used in [**4**] to determine the local blow-up profile for a semilinear heat equation.

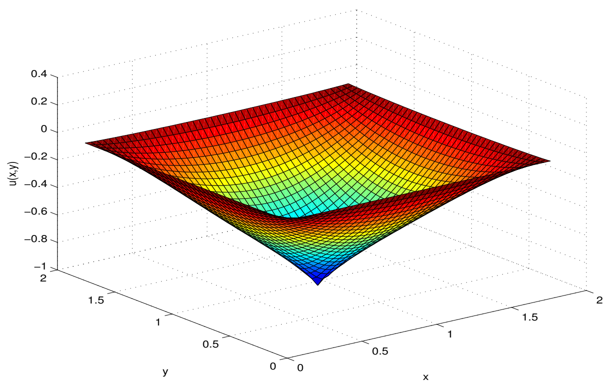


(a) $u$ versus $(x, y)$

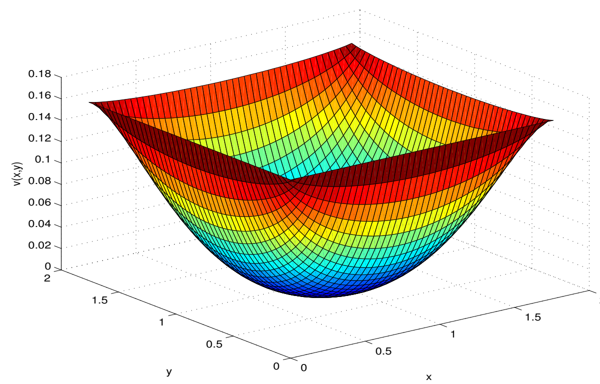


(b) $v$ versus $(x, y)$

FIGURE 16. Experiment 4: for the square $[0, \sqrt{\pi}] \times [0, \sqrt{\pi}]$, and $\lambda = 2.0$ we show touchdown behavior. For the discrete scheme we used $N = 150$ meshpoints in the $x$ and $y$ directions, and a time-step of $\Delta t = 0.15 \times 10^{-4}$. Left figure: $u$ versus $(x, y)$ at $t = 0.1975$. Right figure: $v$ versus $(x, y)$ at the same time.

We now briefly outline the results that can be derived this way. The first step is to introduce new variables by

$$u = -1 + (T-t)^{1/3} w\,(y, s)\,, \qquad s \equiv -\log(T-t)\,, \qquad y \equiv x/\sqrt{T-t}\,. \tag{3.30}$$

With this transformation, (1.1) becomes

$$w_s = \frac{1}{\rho}\nabla \cdot (\rho \nabla w) + \frac{w}{3} - \frac{\lambda}{w^2}\,, \qquad \rho \equiv e^{-|y|^2/4}\,. \tag{3.31}$$

The touchdown profile as $t \to T^-$ is determined by the large $s$ behavior of (3.31). For $s \gg 1$ and $|y|$ bounded, we have that $w = w_\infty + v$, where $v \ll 1$ and $w_\infty \equiv (3\lambda)^{1/3}$. Keeping the quadratic terms in $v$, we get

$$v_s = \frac{1}{\rho}\nabla \cdot (\rho \nabla w) + v + \gamma v^2 + O(v^3)\,, \qquad \gamma = -(3\lambda)^{-1/3}\,. \tag{3.32}$$

As shown in [**4**] (see also [**5**]), the nullspace of the linearized operator in (3.32) is three-dimensional when $N = 2$ and is one-dimensional when $N = 1$. By projecting the nonlinear term in (3.32) against the nullspace of the linearized operator, the following far-field behavior of $v$ for $s \to +\infty$ and $|y|$ bounded was obtained (see (1.7), (1.8) of [**4**]):

$$v \sim \frac{1}{4\gamma s}\left(1 - y^2/2\right)\,, \quad N = 1\,; \qquad v \sim \frac{1}{2\gamma s}\left(1 - |y|^2/2\right)\,, \quad N = 2\,. \tag{3.33}$$

The local touchdown profile is then obtained from $w \sim w_\infty + v$, (3.30) and (3.33), which yields

$$u \sim -1 + [3\lambda(T-t)]^{1/3}\left(1 - \frac{N}{4|\log(T-t)|} + \frac{|x|^2}{8(T-t)|\log(T-t)|}\right)\,. \tag{3.34}$$

By making a binomial approximation on (3.26), it is easy to see that (3.26) agrees asymptotically with (3.34). A rigorous derivation of (3.34) for the case $N = 1$, using this type of center manifold analysis, was given in [**5**]. We also remark that the spatially independent term in (3.34) was proved rigorously in [**3**].

## 4 Touchdown behavior: Variable Permittivity

In this section we obtain some numerical and formal asymptotic results for touchdown behavior associated with a spatially variable permittivity profile in a slab domain. With the transformation

$$v = \frac{1}{3\lambda}(1+u)^3\,, \tag{4.1}$$

the problem (1.1) for $u$ in the slab domain, with permittivity profile $f(x)$, transforms exactly to

$$v_t = v_{xx} - \frac{2}{3v}v_x^2 - f(x)\,, \quad |x| < \frac{1}{2}\,; \qquad v = \frac{1}{3\lambda}\,, \quad x = \pm\frac{1}{2}\,; \qquad v = \frac{1}{3\lambda}\,, \quad t = 0\,, \tag{4.2}$$

We now use the formal power series method of §3.2 to locally construct a power series solution to (4.2) near the unknown touchdown point $x_0$ and the unknown touchdown time $T$. We first assume that $f(x)$ is analytic at $x = x_0$ with $f(x_0) > 0$, so that for $x - x_0 \ll 1$ it has the convergent series expansion

$$f(x) = f_0 + f_0^{'}(x-x_0) + \frac{f_0^{''}(x-x_0)^2}{2} + \cdots\,, \tag{4.3}$$

where $f_0 \equiv f(x_0)$, $f_0^{'} \equiv f^{'}(x_0)$, and $f_0^{''} \equiv f^{''}(x_0)$. Near $x = x_0$, we look for a touchdown profile for (4.2) in the form

$$v(x,t) = v_0(t) + \frac{(x-x_0)^2}{2!}v_2(t) + \frac{(x-x_0)^3}{3!}v_3(t) + \frac{(x-x_0)^4}{4!}v_4(t) + \cdots\,. \tag{4.4}$$

In order for $v$ to be a touchdown profile, it is clear that we must require that

$$\lim_{t\to T^-} v_0 = 0\,; \qquad v_0 > 0\,, \quad \text{for } t < T\,; \qquad v_2 > 0\,, \quad \text{for } t - T \ll 1\,. \tag{4.5}$$

Substituting (4.4) and (4.3) into (4.2), we equate powers of $x - x_0$ to obtain

$$v_0^{'} = -f_0 + v_2\,; \qquad v_2^{'} = -\frac{4v_2^2}{3v_0} + v_4 - f_0^{''}\,; \qquad v_3 = f_0^{'}\,. \tag{4.6}$$

As in §3.2, we assume that $v_2 \ll 1$ and $v_4 \ll 1$ as $t \to T^-$. This yields that $v_0 \sim f_0(T-t)$, and

$$v_2^{'} \sim -\frac{4v_2^2}{3f_0(T-t)} - f_0^{''}\,. \tag{4.7}$$

For $t \to T^-$, we obtain from a simple dominant balance argument that

$$v_2 \sim -\frac{3f_0}{4\left[\log(T-t)\right]} + \cdots\,, \quad \text{as } t \to T^-\,. \tag{4.8}$$

By substituting (4.8) into (4.6) for $v_0$ and integrating the resulting expression we obtain

$$v_0 \sim f_0\,(T-t) + \frac{-3f_0(T-t)}{4|\log(T-t)|} + \cdots\,, \quad \text{for } t \to T^-\,. \tag{4.9}$$

Next, we substitute (4.8), (4.9), and (4.6) for $v_3$, into (4.4) to obtain the local touchdown behavior

$$v \sim f_0\,(T-t)\left[1 - \frac{3}{4|\log(T-t)|} + \frac{3(x-x_0)^2}{8(T-t)|\log(T-t)|} + \frac{f_0^{'}(x-x_0)^3}{6f_0(T-t)} + \cdots\right]\,, \tag{4.10}$$

for $(x - x_0) \ll 1$ and $t - T \ll 1$. Finally, using the nonlinear mapping (4.1) relating $u$ and $v$, we conclude that

$$u \sim -1 + [3f_0\lambda(T-t)]^{1/3}\left(1 - \frac{3}{4|\log(T-t)|} + \frac{3(x-x_0)^2}{8(T-t)|\log(T-t)|} + \frac{f_0^{'}(x-x_0)^3}{6f_0(T-t)} + \cdots\right)^{1/3}\,. \tag{4.11}$$

Here $f_0 \equiv f(x_0)$ and $f_0^{'} \equiv f^{'}(x_0)$.

Since $f(x) > 0$ for the exponential profile $f(x) = e^{\alpha(x^2-1/4)}$ of (2.16 $a$), then (4.11) holds for some touchdown point

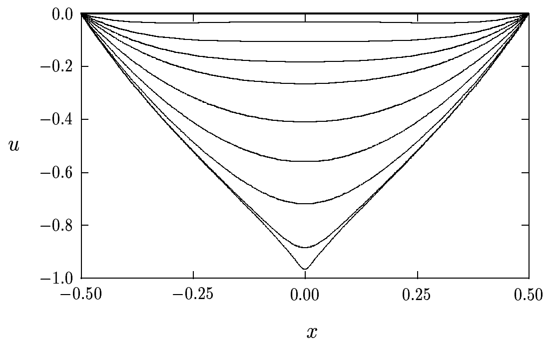


(a) $\alpha = 2.0$, $\lambda = 5.0$

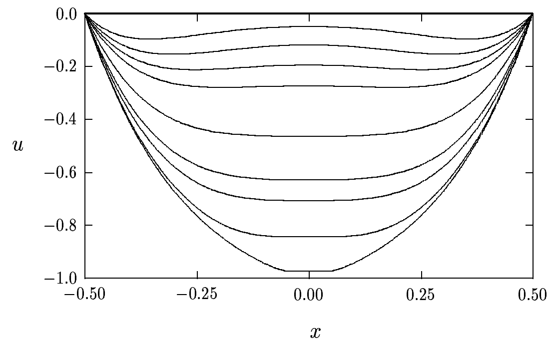


(b) $\alpha = 10.0$, $\lambda = 22.0$

FIGURE 17. Exponential permittivity profile: Left figure: plot of $u$ versus $x$ at different times for $\alpha = 2.0$ and $\lambda = 5.0$. The touchdown time is $T_* \approx 0.1332$ and $\lambda_* \approx 2.14$. Right figure: plot of $u$ versus $x$ at different times for $\alpha = 10.0$ and $\lambda = 22.0$. The touchdown time is $T_* \approx 0.1497$ and $\lambda_* \approx 10.4$. For both cases, the touchdown point is $x_0 = 0$.

$x_0$ and touchdown time $T$. If the touchdown point is at $x_0 = 0$, then (4.11) holds for $f_0 = e^{-\alpha/4}$, and $f_0' = 0$. For two sets of $\alpha$ and $\lambda$, in Fig. 17 we plot the numerically computed $u$ versus $x$ at different times showing touchdown behavior for the exponential permittivity profile. The bounds $T_1$ and $T_2$ on the touchdown time, given in (3.8) and (3.14), together with the numerically computed touchdown time $T_*$ and saddle-node value $\lambda_*$ are as follows:

$$\alpha = 2.0\,, \quad \lambda = 5.0\,; \qquad \lambda_* \approx 2.14\,, \quad T_1 = 0.1697\,, \quad T_2 = 0.4030\,, \quad T_* \approx 0.1332\,, \tag{4.12 a}$$

$$\alpha = 10.0\,, \quad \lambda = 22.0\,; \qquad \lambda_* \approx 10.40\,, \quad T_1 = 0.5321\,, \quad T_2 = 0.3281\,, \quad T_* \approx 0.1497\,. \tag{4.12 b}$$

In obtaining (4.12) we discretized (4.2) in a similar manner as in (3.28). The discrete approximation to $u$ was then obtained from (4.1). The computations were done with a time-step of $\Delta t = 0.6 \times 10^{-5}$ and with $N = 200$ meshpoints, so that $h = 0.4975 \times 10^{-2}$. From Fig. 17 we observe that touchdown occurs at $x_0 = 0$. For $\alpha = 10$, the touchdown profile is much flatter than that for $\alpha = 2$. This is because $f(0) = e^{-\alpha/4}$ is a decreasing function of $\alpha$.

We remark that the touchdown profile (4.11) also holds for the power-law profile $f(x) = |2x|^\alpha$ of (2.16 $a$) whenever the touchdown point $x_0$ is not at the origin, i.e. $x_0 \neq 0$. If this occurs, then (4.11) holds with

$$f_0 = |2x_0|^\alpha\,, \qquad f_0' = 2\alpha|2x_0|^{\alpha-1}\,. \tag{4.13}$$

In Fig. 18 we plot the numerically computed $u$ versus $x$ at different times, and for different sets of $\alpha$ and $\lambda$, showing touchdown behavior for the power law profile. In this figure, the touchdown time $T_*$, and the saddle-node value $\lambda_*$, is shown for each parameter set. From these numerical results, we observe that touchdown seems to occur at two points, symmetrically located about the origin. For each of the computations, we have taken $N = 200$ meshpoints, so that $h = 0.4975 \times 10^{-2}$, and a time step $\Delta t = 0.6 \times 10^{-5}$.

Next, we perform a more delicate computational experiment to determine whether touchdown can occur at $x = 0$ for the power-law profile. We take $\alpha = 0.01$, and $\lambda = 2.0$. Since $\alpha \ll 1$, this example represents a small perturbation of the constant permittivity profile $f(x) \equiv 1$. Using $N = 800$ meshpoints, in Fig. 19 we plot $u$ versus $x$ at $t = 0.34213$ in a neighborhood of the origin. The touchdown time is found to be $T_* \approx 0.3422$. From this figure, we observe that touchdown does not occur at $x = 0$. These computational results suggest the possibility that touchdown cannot occur

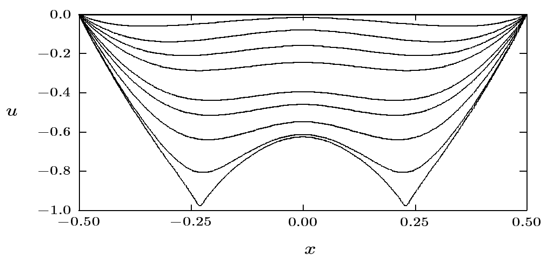

(a) $\alpha = 1.0$, $\lambda = 10.0$

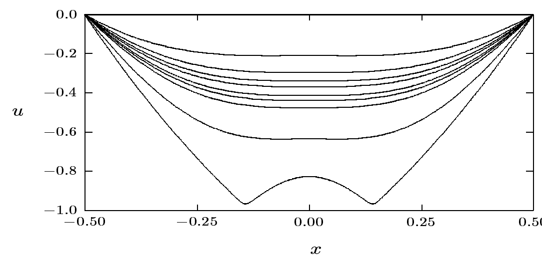

(b) $\alpha = 1.0$, $\lambda = 4.5$

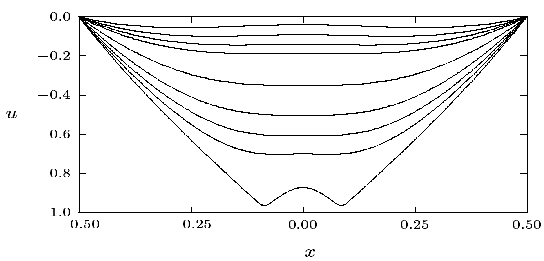

(c) $\alpha = 0.4$, $\lambda = 4.0$

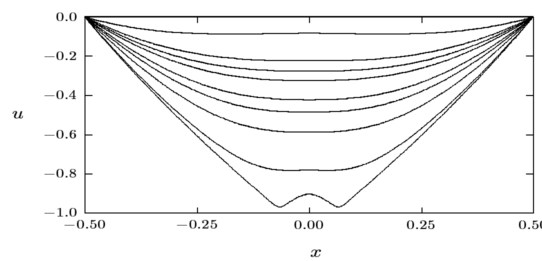

(d) $\alpha = 0.4$, $\lambda = 3.0$

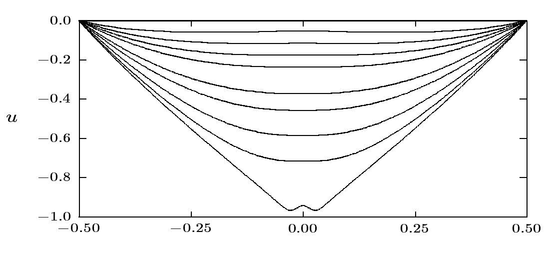

(e) $\alpha = 0.16$, $\lambda = 3.5$

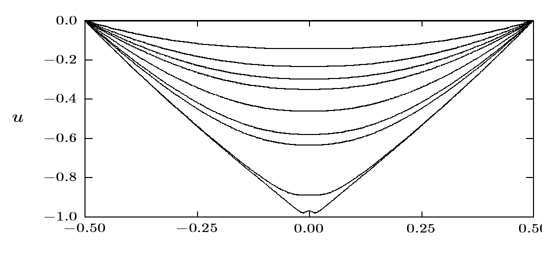

(f) $\alpha = 0.16$, $\lambda = 2.0$

FIGURE 18. Power-law permittivity profile: plots of $u$ versus $x$ at different times for the values of $\alpha$ and $\lambda$ shown in the figure captions. The values for saddle-node point $\lambda_*$, the touchdown time $T_*$, and the touchdown points $x_0$ are as follows: Top left: $\lambda_* \approx 4.2$, $T_* \approx 0.1257$, $x_0 = \pm 0.226$. Top right: $\lambda_* \approx 4.2$, $T_* \approx 1.887$, $x_0 = \pm 0.147$. Middle left: $\lambda_* \approx 2.41$, $T_* \approx 0.2366$, $x_0 = \pm 0.087$. Middle right: $\lambda_* \approx 2.41$, $T_* \approx 0.4857$, $x_0 = \pm 0.067$. Bottom left: $\lambda_* \approx 1.77$, $T_* \approx 0.174$, $x_0 = \pm 0.027$. Bottom right: $\lambda_* \approx = 1.77$, $T_* \approx 0.746$, $x_0 = \pm 0.012$.

at a point $x_0$ where $f(x_0) = 0$. We first investigate this possibility by using a formal power series analysis. Then, at the end of this section we prove a result in this direction. A consequence of this analysis is that touchdown at $x_0 = 0$ is impossible for the power-law profile $f(x) = |2x|^\alpha$.

We first assume that $f(x)$ is analytic at $x = 0$, with $f(0) = 0$ and $f^{'}(0) = 0$, so that $f(x) = f_0 x^2 + O(x^3)$ as $x \to 0$ with $f_0 > 0$. We then look for a power series solution to (4.2) as in (4.4). In place of (4.6) for $v_3$, we get $v_3 = 0$, and

$$v_0^{'} = v_2 \,, \qquad v_2^{'} = -\frac{4v_2^2}{3v_0} + v_4 - 2f_0 \,. \tag{4.14}$$

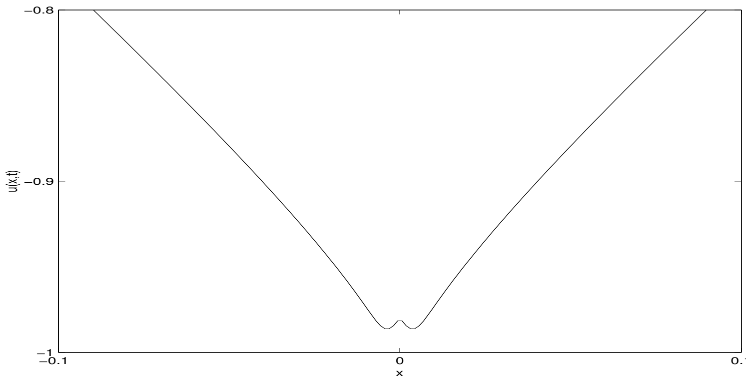


FIGURE 19. Plot of $u$ versus $x$ at $t = 0.34213$ near the touchdown region for the power-law profile with $\alpha = 0.01$ and $\lambda = 2.0$. Touchdown does not occur at $x = 0$, but rather at two points on either side of $x = 0$. The touchdown time is $T_* \approx 0.3422$.

Assuming that $v_4 \ll 1$ as before, we can combine the equations in (4.14) to get

$$v_0^{''} = -\frac{4\left(v_0^{'}\right)^2}{3v_0} - 2f_0 \,. \tag{4.15}$$

By solving (4.15) with $v_0(T) = 0$, we obtain the exact solution

$$v_0 = -\frac{3f_0}{11}(T-t)^2 \,, \qquad v_2 = \frac{6f_0}{11}(T-t) \,. \tag{4.16}$$

Since the criteria (4.5) are not satisfied, the form (4.16) does not represent a touchdown profile centered at $x = 0$.

A similar calculation can be done for the case where $f(x)$ is analytic at $x = 0$, with $f(0) = 0$ and $f'(0) = f_0 > 0$. From a power series expansion solution centered at $x = 0$, and assuming that $v_4 \ll 1$, we get $v_3 = f_0$ and

$$v_0^{''} = -\frac{4\left(v_0^{'}\right)^2}{3v_0} \,, \qquad v_2 = v_0^{'} \,. \tag{4.17}$$

In terms of some constant $A$, the explicit solution to (4.17) with $v_0(T) = 0$ is

$$v_0 = A\,(T-t)^{3/7} \,, \qquad v_2 = -\frac{3A}{7}\,(T-t)^{-4/7} \,. \tag{4.18}$$

Since $v_0$ and $v_2$ have opposite signs as $t \to T^-$, the criteria (4.5) do not hold, and we do not have touchdown at $x = 0$. These formal calculations suggest the general result that touchdown cannot occur at a point $x = x_0$ where $f(x_0) = 0$. Without loss of generality, we assume that $x_0 = 0$. Our final result is as follows:

**Theorem 4.1**: *Let $u(x,t)$ be a solution of*

$$u_t = u_{xx} - \frac{\lambda f(x)}{u^2} \,, \qquad |x| \le \frac{1}{2} \,, \quad 0 < t < T \,; \qquad u\left(\pm\frac{1}{2}, t\right) = 1 \,, \qquad u(x,0) = 1 \,. \tag{4.19}$$

*Here $f(x)$ satisfies (2.7), and $u$ touches down at the finite time $T$. If $f(0) = 0$, then $x_0 = 0$ cannot be a touchdown point of $u(x,t)$ at finite time $T$.*

**Proof:** Set $v = u_t$. Then, we calculate

$$v_t = v_{xx} + \frac{2\lambda f(x)}{u^3} v \,, \qquad |x| \le \frac{1}{2} \,, \quad 0 < t < T \,; v\left(\pm\frac{1}{2}, t\right) = 0 \,, \qquad v(x,0) \le 0 \,. \tag{4.20}$$

Here $\frac{2\lambda f(x)}{u^3}$ is a locally bounded function. By the strong maximum principle, we conclude that

$$u_t = v < 0 \,, \qquad |x| < \frac{1}{2} \,, \quad 0 < t < T \,. \tag{4.21}$$

Therefore, since $f(0) = 0$, we have as $t \to T^-$ that $u_{xx} = u_t < 0$ at $x = 0$. From this result, and from the smoothness of $u(x,t)$, we deduce that when $t \to T^-$, there exists an $\bar{x} \neq 0$ such that $u(0,t) > u(\bar{x},t)$. This shows that $x_0 = 0$ cannot be a touchdown point of $u(x,t)$ at finite time $T$. ■

## 5 Conclusion

We have analyzed some properties of the pull-in voltage instability for (1.1) in terms of a spatially variable dielectric permittivity profile for the thin elastic membrane. Bounds on the pull-in voltage were given in §2, and sufficient conditions for finite-time touchdown were obtained in §3, together with bounds on the touchdown time. From these bounds, and from numerical computations, it was shown that by appropriately tailoring the dielectric permittivity of the thin membrane the pull-in voltage and the pull-in distance can both be increased. For the special case of a power-law permittivity profile in a slab domain, this conclusion was first obtained in [**14**]. For voltages that exceed the pull-in voltage threshold, the local touchdown profile was calculated asymptotically in §3 and §4 for spatially uniform and spatially nonuniform permittivity profiles, respectively.

An interesting open problem is to formulate an optimization problem for the pull-in distance associated with the steady-state problem (1.1), whereby an optimum permittivity profile $f$ can be computed numerically for a given set of design constraints on both the stable operating range of the applied voltage and maximum value of $V$ that is available by the power supply.

Another way of tailoring the pull-in voltage, without introducing a spatially nonuniform permittivity profile, is to rigidly attach the thin membrane near the region where the deflection would otherwise be largest. Mathematically this corresponds to considering (1.1) with $f(x,y) \equiv 1$, in a domain $\Omega$ punctured by a small patch $\Omega_\varepsilon$ of area $O(\varepsilon^2) \ll 1$, where $u = 0$ for $x \in \Omega_\varepsilon$. An asymptotic theory for the location of saddle-node bifurcation values for general classes of semilinear problems in such singularly perturbed domains was developed in [**18**]. For a MEMS device, symmetry breaking properties of radially symmetric solutions for an annular domain were computed numerically in [**15**]. For this type of modification of (1.1), it would be interesting to obtain an analytical theory for the pull-in voltage instability.

Finally, it would be interesting to analyze pull-in voltage and touchdown behavior for extensions of the basic model (1.1) whereby the upper surface is modeled by an elastic plate of nonzero rigidity and inertial effects are considered. The resulting model for the deflection of a thin plate that has a spatially uniform permittivity profile involves the Biharmonic operator $\Delta^2$ and takes the following form for some $\beta > 0$ and $\delta > 0$ (see equation (7.50) of [**13**]):

$$\beta \frac{\partial^2 u}{\partial t^2} + \frac{\partial u}{\partial t} - \Delta u + \delta \Delta^2 u = -\frac{\lambda}{(1+u)^2}\,, \quad x \in \Omega\,; \qquad u = 0\,, \quad (x,y) \in \partial\Omega\,; \qquad u(x,y,0) = 0\,. \tag{5.1}$$

## Appendix A Derivation of the Membrane Deflection Equation

Following the analysis in [**14**] and [**6**], we now outline the derivation of the membrane deflection equation (1.1). Referring to Fig. 1, the electrostatic potential is assumed to satisfy Laplace's equation in the gap between the fixed plate and the lower surface of the membrane. Inside the thin membrane, the dielectric permittivity $\varepsilon_2 = \varepsilon_2(x,y)$ can exhibit a spatial variation. On the upper surface of the membrane, a fixed voltage $V$ is imposed. Therefore, in dimensionless variables, the problem for the electrostatic potential is

$$\frac{\partial^2\psi}{\partial z^2} + \delta^2 \left( \frac{\partial^2\psi}{\partial x^2} + \frac{\partial^2\psi}{\partial y^2} \right) = 0\,, \quad (x,y) \in \Omega\,, \quad 0 \le z \le \hat{u} - l\,, \tag{A.1 a}$$

$$\varepsilon_2 \frac{\partial^2\psi}{\partial z^2} + \delta^2 \left( \frac{\partial}{\partial x} \left( \varepsilon_2 \frac{\partial\psi}{\partial x} \right) + \frac{\partial}{\partial y} \left( \varepsilon_2 \frac{\partial\psi}{\partial y} \right) \right) = 0\,, \quad (x,y) \in \Omega\,, \quad \hat{u} - l \le z \le \hat{u} + l\,, \tag{A.1 b}$$

$$\psi = 0\,, \quad z = 0 \text{ (ground plate)}, \qquad \psi = 1\,, \quad z = \hat{u} + l \text{ (upper membrane surface)}\,, \tag{A.1 c}$$

together with the continuity of the potential and the displacement fields across $z = \hat{u} - l$. Here $\psi$ is the dimensionless potential scaled with respect to the applied voltage $V$, $x$ and $y$ are scaled with respect to the length $L$ of the undeformed plate $\Omega$, $z$ is a vertical coordinate scaled with respect to the undeformed gap-size $d$, $2l$ is the thickness of the membrane, and $\delta \equiv d/L \ll 1$ is the device aspect ratio. The deflection of the membrane is denoted by $\hat{u}$, with $\hat{u} = 1$ on $\partial\Omega$ denoting the undeflected state. Note that $\hat{u} = 0$ corresponds to the touching of the membrane and the lower plate and that $\hat{u}$ is scaled in the same manner as $z$.

In the small aspect ratio limit $\delta \ll 1$, the asymptotic solution for $\psi$ that is continuous across $z = \hat{u} - l$ is

$$\psi = \begin{cases} \psi_L \frac{z}{\hat{u}-l}\,, & 0 \le z \le \hat{u} - l\,, \\ 1 + \frac{(1-\psi_L)}{2l} \left( z - (\hat{u} + l) \right)\,, & \hat{u} - l \le z \le \hat{u} + l\,. \end{cases} \tag{A.2}$$

To ensure that the displacement field is continuous across $z = \hat{u} - l$ to leading order in $\delta$, we must impose that $\varepsilon_0 \psi_z|_- = \psi_2 \psi_z|_+$, where the plus or minus signs indicate that $\psi_z$ is to be evaluated on the upper or lower side of the bottom surface $z = \hat{u} - l$ of the membrane, respectively. This condition determines $\psi_L$ in(A.2) as

$$\psi_L = \left[ 1 + \frac{2l}{\hat{u} - l} \left( \frac{\varepsilon_0}{\varepsilon_2} \right) \right]^{-1}\,. \tag{A.3}$$

From (A.2) and (A.3), the electric field in the $z$-direction inside the membrane is independent of $z$, and is given by

$$\psi_z = \frac{\varepsilon_0}{\varepsilon_2(\hat{u} - l)} \left[ 1 + \frac{2l}{\hat{u} - l} \frac{\varepsilon_0}{\varepsilon_2} \right]^{-1} \sim \frac{\varepsilon_0}{\varepsilon_2 \hat{u}}\,, \quad \text{for } l \ll 1\,. \tag{A.4}$$

The coupling of the electrostatic field to the deflection of the membrane was modeled in [**6**] by a dimensionless damped wave equation of the form

$$\gamma^2 \frac{\partial^2 \hat{u}}{\partial t^2} + \frac{\partial \hat{u}}{\partial t} - \Delta \hat{u} = -\lambda \left( \frac{\varepsilon_2}{\varepsilon_0} \right) \left[ \delta^2 |\nabla_\perp \psi|^2 + (\frac{\partial \psi}{\partial z})^2 \right], \quad (x,y) \in \Omega\,, \quad \hat{u} - l \le z \le \hat{u} + l\,. \tag{A.5}$$

Here $\lambda$ is defined in (1.2), the time $t$ is scaled with respect to the strength of the damping, and $\nabla_\perp$ denotes the gradient in the $x$ and $y$ directions only. By substituting (A.4) into (A.5), and letting $\delta \ll 1$, we obtain

$$\gamma^2 \frac{\partial^2 \hat{u}}{\partial t^2} + \frac{\partial \hat{u}}{\partial t} - \Delta \hat{u} \sim -\lambda \frac{\varepsilon_0}{\varepsilon_2 \hat{u}^2}\,, \quad (x,y) \in \Omega\,; \qquad \hat{u} = 1\,, \quad (x,y) \in \partial\Omega\,. \tag{A.6}$$

We then define $u \equiv \hat{u} - 1$, so that $u = 0$ is the undeflected state. Finally, assuming that the damping force dominates the inertial force so that $\gamma \ll 1$, as was done in [**6**], (A.6) reduces to the membrane deflection equation (1.1) of §1.

**Acknowledgements**

M. J. W. gratefully acknowledges the support by NSERC under grant 81541.

## References


[1] U. Ascher, R. Christiansen, R. Russell, *Collocation Software for Boundary Value ODE's*, Math. Comp., **33**, (1979), pp. 659-679.

[2] R. E. Bank, *PLTMG: A Software Package for Solving Elliptic Partial Differential Equations*, User's guide 8.0, Software, Environments, and Tools, SIAM, Philadelphia, PA, (1998), xi+110 pages.

[3] M. Fila, J. Hulshof, *A Note on the Quenching Rate*, Proc. Amer. Math. Soc., **112**, No. 2, (1991), pp. 473–477.

[4] S. Filippas, R. V. Kohn, *Refined Asymptotics for the Blow Up of* $u_t - \Delta u = u^p$, Comm. Pure Appl. Math. **45**, No. 7, (1992), pp. 821–869.

[5] S. Filippas, J. S. Guo, *Quenching Profiles for One-Dimensional Semilinear Heat Equations*, Quart. Appl. Math., **51**, No. 4, (1993), pp. 713–729.

[6] G. Flores, G. A. Mercado, J. A. Pelesko, *Dynamics and Touchdown in Electrostatic MEMS*, Proceedings of ICMENS 2003, (2003), pp. 182-187.

[7] J. S. Guo, *On the Quenching Behavior of the Solution of a Semilinear Parabolic Equation*, J. Math. Anal. Appl., **151**, No. 1, (1990), pp. 58–79.

[8] J. B. Keller, J. Lowengrub, *Asymptotic and Numerical Results for Blowing-Up Solutions to Semilinear Heat Equations*, Singularities in Fluids, Plasmas, and Optics (Heraklion 1992), pp. 11-38, NATO Adv. Sci. Inst. Ser. C Math. Phys. Sci. 404, Kluwer Acad. Publ. Dordrecht, (1993)

[9] K. W. Morton, D. F. Mayers, *Numerical Solution of Partial Differential Equations*, Cambridge University Press, Cambridge, U.K. (1994).

[10] H. C. Nathanson, W. E. Newell, R. A. Wickstrom, J. R. Davis, *The Resonant Gate Transistor*, IEEE Trans. on Elect. Devices, **14**, (1967), pp. 117–133.

[11] J. A. Pelesko, *Multiple Solutions in Electrostatic MEMS*, Proceedings of MSM 2001, Hilton Head, South Carolina, (2001), pp. 290-293.

[12] J. A. Pelesko, A. A. Triolo, *Nonlocal Problems in MEMS Device Control*, J. Eng. Math., **41**, No. 4, (2001), pp. 345–366.

[13] J. A. Pelesko, D. H. Bernstein, *Modeling MEMS and NEMS*, Chapman Hall and CRC Press, (2002).

[14] J. A. Pelesko, *Mathematical Modeling of Electrostatic MEMS with Tailored Dielectric Properties*, SIAM J. Appl. Math., **62**, No. 3, (2002), pp. 888–908.

[15] J. A. Pelesko, D. Bernstein, J. McCuan, *Symmetry and Symmetry Breaking in Electrostatic MEMS*, Proceedings of MSM 2003, (2003), pp. 304–307.

[16] I. Stackgold, *Green's Functions and Boundary Value Problems*, Wiley, New York, (1998).

[17] G. I. Taylor, *The Coalescence of Closely Spaced Drops when they are at are at Different Electric Potentials*, Proc. Roy. Soc. A, **306**, (1968), pp. 423–434.

[18] M. J. Ward, W. D. Henshaw, J. B. Keller, *Summing Logarithmic Expansions for Singularly Perturbed Eigenvalue Problems*, SIAM J. Appl. Math. **53**, No. 3, (1993), pp. 799-828.